Available online at www.sciencedirect.com
SCIENCE DIRECT®
Journal of Computational Physics 196 (2004) 490–538
JOURNAL OF COMPUTATIONAL PHYSICS
www.elsevier.com/locate/jcp

Modelling detonation waves in heterogeneous energetic materials

Ashwin Chinnayya [a,b,*], Eric Daniel [a,b], Richard Saurel [a,b,c]

[a] Polytech Marseille, UMR CNRS 6595-IUSTI, 5 rue E. Fermi, 13453 Marseille Cedex 13, France
[b] INRIA Projet SMASH, 2004 route des Lucioles, 06902 Sophia Antipolis, France
[c] Institut Universitaire de France, 103, boulevard St. Michel, 75005 Paris, France

Received 3 March 2003; received in revised form 6 November 2003; accepted 11 November 2003

Abstract

The computation of detonation waves in heterogeneous explosives involves compressible multiphase mixtures due to the chemical decomposition of the energetic material as well as its heterogeneous initial formulation. Also material interfaces are present between the explosive and the surrounding inert or reactive materials. We develop a new method for the modelling of interface problems and multiphase mixtures in the particular limit where phases pressures and velocities relax towards equilibrium very fast. This method is a variant of the discrete equations for multiphase mixtures proposed by Abgrall and Saurel [J. Comput. Phys. 186 (2) (2003) 361]. The new discrete model is adapted to reacting flows with mass, momentum and energy transfer. The model is based on the pure material equation of state only (no mixture equation of state is used) for the computation of the reaction zone of detonation waves. The algorithm is full Eulerian and fulfills interface conditions between mixtures and pure materials automatically. It is validated over a set of difficult test problems with exact solution and its multi-dimensional capabilities are shown over problems involving a large number of materials.

AMS: 65Z05; 76T10; 76M12

Keywords: Multiphase flows; Non-conservative hyperbolic system; Detonation waves; Interfaces; Godunov type methods

1. Introduction

Computation of detonation waves in condensed energetic materials involves many fundamental problems. Among them, two are related to continuum mechanics and thermodynamics modelling and numerical resolution. The first one is due to the multiphase feature of the condensed energetic material involving several compressible phases (solid and gas). The second problem is related to the presence of material

* Corresponding author. Present address: CORIA – UMR CNRS 6614, Avenue de l'Université, Université de Rouen, Site Universitaire du Madrillet BP 12, 76801 Saint Etienne du Rouvray cedex, France. Tel.: +33-2-32-95-36-51; fax: +33-2-32-91-04-85.
E-mail addresses: Ashwin.Chinnayya@coria.fr (A. Chinnayya), Eric.Daniel@polytech.univ-mrs.fr (E. Daniel), Richard.Saurel@polytech.univ-mrs.fr (R. Saurel).

0021-9991/$ - see front matter
doi:10.1016/j.jcp.2003.11.015

interfaces. Indeed, the explosive is always confined by other inert materials and the detonation dynamics depends on the interactions of the various waves propagating into the explosive mixture and interacting with the surrounding materials. These interface problems require an accurate numerical treatment.

Regarding the first problem, the multiphase feature is due to the decomposition of the condensed phase to gaseous products. So, this mixture has a physico-chemical origin. Determination of the basic thermodynamic properties of this mixture imply many difficulties. Usually, the basic flow model is composed of the Euler equations augmented by several species conservation equations. Closing this kind of model requires an equation of state (EOS) for the mixture, which is based on the pure substances EOS. The EOS for the condensed material is of Mie–Gruneisen type, whose parameters are determined from the experimental Hugoniot curve. Regarding the gas phase equation of state, two instances have to be considered.

If the reaction is very fast, the reaction zone is very thin (a few microns) and the available mechanical energy for propulsion devices is low compared to the one of the gas products outside the reaction zone. This is the case for most conventional applications. The reaction zone has to be resolved because it is responsible for the detonation dynamics, but a detailed description of this zone is not necessary. A reduced gas phase equation of state of Mie–Gruneisen type can be determined easily with the help of thermochemical codes [4,16].

As soon as the two equations of state for pure substances (solid and gas) are available, it is possible to build the equation of state of the mixture, also of Mie–Gruneisen type. But two equilibrium assumptions between the two phases are needed: pressure and temperature equilibrium or pressure and density equilibrium, etc. These types of thermodynamic closure assumptions suffer from a lack of physical validity.

In the case of thick reaction zones (from 1 mm up to 1 m), an accurate determination of the flow variables in this zone is mandatory. The multi-component reactive material contains several solid chemical species that consume with very different characteristic times, yielding a multi-component solid–gas mixture whose composition varies strongly. This is a non-equilibrium phenomenon, non-isentropic, and that cannot be computed with a thermo-chemical code. The thermodynamic gas properties must be computed with a theoretical equation of state (BKW, virial expansions), which requires the knowledge of the gas composition and its thermodynamic variables (internal energy, density). These thermodynamic variables are not available with conventional flow models because only the mixture energy and density can be computed from the Euler equations. Thus, it is necessary to adopt another flow model.

Another reason for not using the Euler equations is that the building of a mixture equation of state is quite impossible when the solid phase is governed by an EOS and the gas phase is governed by another EOS, which is function of gas thermodynamic variables and gas composition.

Consequently, our first motivation for a multiphase flow model for detonations is based on mixture thermodynamics considerations. This was underlined in [3,9,21,22,31,32,34].

Consider now the second problem involving interfaces between compressible materials. An explosive is always confined by other inert materials. It is important to determine accurately the propulsive effects that have strong coupling effects with the detonation dynamics. This second topic poses fundamental computational challenges related to the creation of artificial fluid mixtures. Such artificial mixtures appear when the interface separating two fluids takes place in an arbitrary position into the computational cell. The thermodynamic properties (equation of state parameters for example) being different from one fluid to the other and function only of the pure fluid thermodynamic variables (density and internal energy) their use with the mixture density and internal energy is problematic. Indeed the Euler equations allow us only the determination of these mixture thermodynamic variables.

With Lagrangian or tracking methods, the interface coincides with the cell boundary. With Eulerian methods, the interface has an arbitrary location inside the cell and extra ingredients have to be introduced into the method or model (or both). In spite of this fundamental difficulty, Eulerian methods are attractive because of their simplicity and efficiency. The second issue addressed by this paper is precisely the computation of interface problems with Eulerian methods.

For the past decade, considerable efforts have been done in this direction. We refer to the papers by Benson [8], Saurel and Abgrall [32] and the references herein for an overview.

The use of Eulerian methods has been initiated by Karni [23], Abgrall [1], Karni [24], Shyue [36], Saurel and Abgrall [32], Fedkiw et al. [14], Saurel and Abgrall [33], Abgrall and Saurel [2]. Two kinds of methods can be exhibited in these references.

Fedkiw's strategy is based on the level set method. The resolution of interface problems and detonations is obtained by the same methodology, which uses ghost cells, mimicking boundary conditions on discontinuities.

The other approach is based on a multiphase modelling of the entire flow [2,33,34]. This approach is more complicated that the previous one because there are much more equations in the system of partial differential equations (PDEs) and non-conservative terms are present. However, this approach allows the determination of the thermodynamics of each phase of the mixture. This method is able to deal with the first goal of this paper, that is to say physical fluid mixtures due to chemical decomposition, as well as artificial mixtures, the second issue. In these references, a model able to deal with physical mixtures as well as with artificial ones was proposed. The non-conservative terms were considered and discretizations based on physical considerations were proposed. The numerical approximations were derived by considering a uniform flow with respect to velocities and pressures of the different phases, and the idea was to keep such wave structure invariant by the scheme. Such approximations are valid for interfaces, which correspond to volume fraction discontinuities in this context. Across an interface, velocities and pressures remain constant, but through a shock wave, the velocities, the pressures and the volume fractions vary. Therefore the corresponding discretization was no longer valid. Also, the method appeared to be too much dissipative on interfaces because the Riemann solver considered only 2 waves instead of 7.

In a recent paper by Abgrall and Saurel [2], these difficulties have been cleared. The key idea is to discretize the multiphase mixture at the microscopic level and then to average the discrete equations. It provides a new discrete model as well as the numerical method. This procedure was called "Discrete Equations Method" (DEM). This is done in the opposite way of what was done before. Indeed, it is conventional to obtain a system of PDEs on the basis of averaging procedures, and then to discretize the corresponding PDE system. Here, we adapt the DEM strategy to the particular context of detonation waves and multimaterial hydrocodes. To do this, the method needs several modifications:

- The materials are reactive and it is necessary to adapt the model to such situation.
- The equations of state are complex and chemical effects need to be modelled and solved accurately.
- Multiphase mixtures encountered in the physics of detonation waves have some specificities: the mixture behaves essentially with a single velocity and pressure [22]. A careful description of phases interaction will lead to relaxation coefficients that will be shown to produce very fast phases pressure and velocity equilibrium.
- The overall model and method need to be extended to an arbitrary number of phases.
- The model will be shown to obey a dissipative inequality.
- The method is extended to two-dimensions by dimensional splitting.
- The extra computational difficulties due to mass transfer, stiff chemical kinetics are explained and solved.

The present paper is organized as follows. First the reactive multiphase model is developed by using conventional averaging procedures and continuous differential operators. Then the DEM is developed on the basis of a microstructure topology representative of an explosive mixture. It provides the basic hyperbolic solver in absence of mass transfer and chemical reactions. This hyperbolic solver corresponds to the cornerstone of the numerical method. But it is also interesting to look at the system of PDEs that are the continuous analogue of these discrete formulas. Such system of PDEs is obtained as the continuous limit of the discrete equations. The analysis of this limit system provides explicit formulas for the averaged interfacial pressures and velocities as well as all relaxation terms. This system is then compared to the one that is obtained initially with the conventional averaging method. Both models have the same structure and the second one contains all mechanical closure relations. The timescales of the various relaxation processes are

analysed and it is shown that in detonation conditions the pressures and velocities relax very fast. Thus a specific algorithm is developed for such situations. The solver stability and positivity properties are analysed. Then a series of test problems and validations is presented.

2. Theoretical model

Advanced continuum mechanics and thermodynamics models of condensed heterogeneous are based on a multiphase description. Indeed, the condensed energetic material is a multiphase mixture of several condensed species with a small percentage of gas. When the decomposition reaction occurs during the detonation process, new gaseous species are produced increasing the multiphase character of the mixture and the production of solid components may not be excluded. As an example, the schematic representation of the detonation process of CHNO-based with aluminum and the different chemical reactions involved are given in Fig. 1. This explosive, confined by inert materials, involves three condensed reactive species: $C_aH_bN_cO_d$, Al and C that decompose under specific reactions, yielding both gaseous and condensed species.

The solid components are ($C_aH_bN_cO_d$, Al, Al_2O_3, C) while the other components belong to the gaseous detonation products. The pure materials EOS depend on the internal composition of the phases meaning the EOSs are function of the density ρ_k, the internal energy of the phase e_k, and the mass fractions $\{Y_{k,m}\}_{m=1,\ldots,N_k}$:$p_k = p_k(\rho_k, e_k, \{Y_{k,m}\}_{m=1,\ldots,N_k})$. Two kinds of EOS are given in Appendices A and B: the H9 EOS [20] specially designed for the description of gaseous detonation products that are induced by CHNO-type explosives and a Mie–Gruneisen multi-component equation of state for the reactive solid material. In this chemical decomposition model, each of these chemical reactions has very different characteristic time. The decomposition of the solid $C_aH_bN_cO_d$ yields gaseous products but also a condensed species C. Combustion of the condensed aluminum needs a gaseous species and produces gas and solid species. Reaction (3) is of the same type, while reaction (4) involves gaseous components only. The burning laws can be function of phase pressure, or phase temperature, or both. This example is well suited to illustrate the multiphase multi-species feature of the kind of explosives considered in this study.

In this section, we develop the necessary multiphase model for an arbitrary number of fluids, an arbitrary number of species and consider mass transfer between phases as well as within phases. This work is done at the continuous level and is close to the models by Baer and Nunziato [3], Kapila et al. [21], Saurel and Le Metayer [34].

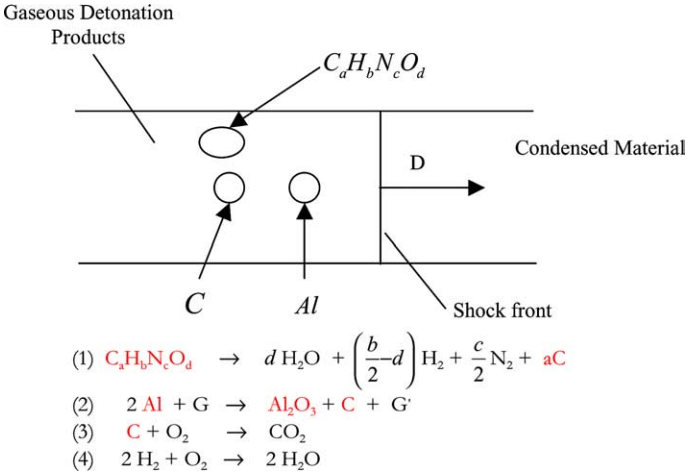

Fig. 1. Schematic representation of a detonation wave and chemical decomposition of a CHNO-based explosive.

The reactive Euler equations in each phase k, $k \in [1, N]$ are first considered. N_k is the number of chemical species composing the phase k and each species m is defined by its mass fraction $Y_{k,m}$. In a single phase (gas, liquid or solid) the mass diffusion is neglected and the velocity of the chemical species is the velocity of the considered phase:

$$\begin{aligned}
&\frac{\partial \rho_k}{\partial t} + \operatorname{div}(\rho_k \vec{u}_k) = 0,\\
&\frac{\partial \rho_k \vec{u}_k}{\partial t} + \operatorname{div}(\rho_k \vec{u}_k \otimes \vec{u}_k) + \nabla p_k = 0,\\
&\frac{\partial \rho_k E_k}{\partial t} + \operatorname{div}((\rho_k E_k + p_k)\vec{u}_k) = 0,\\
&\frac{\partial \rho_k Y_{k,m}}{\partial t} + \operatorname{div}(\rho_k Y_{k,m} \vec{u}_k) = \dot{\omega}_{k,m} \quad \text{for } m \in [1, N_k].
\end{aligned} \tag{2.1}$$

The internal energy of each fluid is $e_k = E_k - (\vec{u}_k \cdot \vec{u}_k)/2$. Each sub-system is closed by a pure phase EOS of the form $p_k = p_k(\rho_k, e_k, \{Y_{k,m}\}_{m=1,\ldots,N_k})$. The last equation expresses the chemical evolution of the mth species within the phase k. The notations are conventional as well as the assumptions about the chemical features of an individual phase. Note that the production term in this equation represents mass production within the kth phase. Within the kth phase, the sum of the mass fractions equals unit. The previous assertion leads to the relation $\sum_{m=1,\ldots,N_k} \dot{\omega}_{k,m} = 0$.

Some reactions occur at the materials interfaces and are involved in mass transfer terms between phases: they cannot appear in these equations without considering the multiphase character of the mixture.

The multiphase flow equations are obtained by using the averaging procedure of Drew and Passman [12]. With this procedure, the pure fluid equations (2.1) are multiplied by an indicator function X_k to select the appropriate fluid, and are then averaged over the two-phase control volume. The indicator function X_k is defined by:

$$X_k(M,t) = \begin{cases} 1 & \text{if } M \text{ belongs to the phase } k,\\ 0 & \text{otherwise.} \end{cases}$$

This function obeys the equation

$$\frac{\partial X_k}{\partial t} + \vec{\sigma} \nabla X_k = 0, \tag{2.2}$$

where $\vec{\sigma}$ represents the *local* interface velocity.

To select the appropriate fluid, Eqs. (2.1) are multiplied by the indicator function X_k and are volume averaged with the operator:

$$\langle f \rangle = \frac{1}{V} \int_V f \, \mathrm{d}V,$$

where f is an arbitrary flow function. We obtain:

$$\begin{aligned}
&\frac{\partial \langle X \rangle_k}{\partial t} + \langle \vec{u} \nabla X \rangle_k = \langle (\vec{u} - \sigma) \nabla X \rangle_k,\\
&\frac{\partial \langle X\rho \rangle_k}{\partial t} + \operatorname{div} \langle X \rho \vec{u} \rangle_k = \langle \rho(\vec{u} - \sigma) \nabla X \rangle_k,\\
&\frac{\partial \langle X\rho \vec{u} \rangle_k}{\partial t} + \operatorname{div} \langle X \rho \vec{u} \otimes \vec{u} \rangle_k + \nabla \langle Xp \rangle_k = \langle p \nabla X \rangle_k + \langle \rho \vec{u} (\vec{u} - \sigma) \nabla X \rangle_k,\\
&\frac{\partial \langle X\rho E \rangle_k}{\partial t} + \operatorname{div} \langle X(\rho E + p)\vec{u} \rangle_k = \langle p \vec{u} \nabla X \rangle_k + \langle \rho E (\vec{u} - \sigma) \nabla X \rangle_k,\\
&\frac{\partial \langle X\rho Y_m \rangle_k}{\partial t} + \operatorname{div} \langle X \rho Y_m \vec{u} \rangle_k = \langle X \dot{\omega}_m \rangle_k + \langle \rho Y_m (\vec{u} - \vec{\sigma}) \nabla X \rangle_k.
\end{aligned} \tag{2.3}$$

In the right-hand side of the species conservation equations, two source terms appear, which are related to chemical reactions within the kth phase, $\langle X\dot{\omega}_m\rangle_k$, and the mass transfer between different phases, $\langle\rho Y_m(\vec{u}-\vec{\sigma})\nabla X\rangle_k$. It is straightforward to obtain the average mass transfer between phases: $\langle\rho(\vec{u}-\vec{\sigma})\nabla X\rangle_k = \sum_{m=1,\ldots,N_k}\langle\rho Y_m(\vec{u}-\vec{\sigma})\nabla X\rangle_k + \sum_{m=1,\ldots,N_k}\langle X\dot{\omega}_m\rangle_k = \sum_{m=1,\ldots,N_k}\langle\rho Y_m(\vec{u}-\vec{\sigma})\nabla X\rangle_k$.

The other terms factor of $(\vec{u}-\sigma)$ represent the momentum transfer due to mass transfer $(\rho\vec{u})(\vec{u}-\sigma)\nabla X$ and the energy transfer due to mass transfer $(\rho E)(\vec{u}-\sigma)\nabla X$.

In the previous equations only the microscopic variables appear. They have to be linked with the macroscopic variables that are more convenient for computations. To do this, we assume that the bulk fluid variables are equal to their averages: $\rho_k = \langle\rho_k\rangle$, $\vec{u}_k = \langle\vec{u}_k\rangle$, $p_k = \langle p_k\rangle$, $e_k = \langle e_k\rangle$. In other words, we neglect internal turbulence.

The term ∇X_k is non-zero only at the interfaces and consequently defines the interface position and its normal at the microscopic level. Then the product $f\nabla X$ defines the value of f at the interfaces and it is noted f_i.

In order to interpret some interfacial terms, the mass transfer is removed in the multiphase system. This is done in the sake of clarity. As a consequence, the interface conditions at the microscopic level reduce to: $p_i = p_k$ and $\vec{u}_i\cdot\nabla X_k = \vec{\sigma}\cdot\nabla X_k = \vec{u}_k\cdot\nabla X_k$.

Due to non-equilibrium effects, interface variables may have fluctuations around an average state, thus: $p_i = \bar{p}_i + \delta p_i$ and $\vec{u}_i = \bar{\vec{u}}_i + \delta\vec{u}_i$ such as $\bar{p}_i = \langle p_i\rangle$ and $\bar{\vec{u}}_i = \langle\vec{u}_i\rangle$.

The averages of the various non-conservative products can be written as,

$$\langle\vec{u}\nabla X\rangle_k = \langle\bar{\vec{u}}_i\nabla X_k\rangle + \langle\delta\vec{u}_i\nabla X_k\rangle = \bar{\vec{u}}_i\nabla\alpha_k + \langle\delta\bar{\vec{u}}_i\nabla X_k\rangle,$$

$$\langle p_k\nabla X_k\rangle = \langle\bar{p}_i\nabla X_k\rangle + \langle\delta p_i\nabla X_k\rangle = \bar{p}_i\nabla\alpha_k + \langle\delta p_i\nabla X_k\rangle,$$

$$\langle(p\vec{u})_k\nabla X_k\rangle = \langle\bar{p}_i\bar{\vec{u}}_i\nabla X_k\rangle + \langle\bar{p}_i\delta\vec{u}_i\nabla X_k\rangle + \langle\delta p_i\bar{\vec{u}}_i\nabla X_k\rangle + \langle\delta p_i\delta\vec{u}_i\nabla X_k\rangle.$$

Note that we used the identity $\langle\nabla X_k\rangle = \nabla\alpha_k$ that implicitly admits that the volume average $\langle X_k\rangle$ represents the volume fraction of the phase k, that is to say α_k.

We note $\dot{\alpha}_k = -\langle\delta\bar{\vec{u}}_i\nabla X_k\rangle$ the rate of change in volume fraction due to non-equilibrium effects and $F_k = \langle\delta p_i\nabla X_k\rangle$ the average pressure drag force. By neglecting the second-order term, the three averaged non-conservative products read:

$$\langle\vec{u}\nabla X\rangle_k = \langle\bar{\vec{u}}_i\nabla X_k\rangle + \langle\delta\vec{u}_i\nabla X_k\rangle = \bar{\vec{u}}_i\nabla\alpha_k - \dot{\alpha}_k,$$

$$\langle p_k\nabla X_k\rangle = \langle\bar{p}_i\nabla X_k\rangle + \langle\delta p_i\nabla X_k\rangle = \bar{p}_i\nabla\alpha_k + F_k,$$

$$\langle(p\vec{u})_k\nabla X_k\rangle = \bar{p}_i\bar{\vec{u}}_i\nabla\alpha_k - \bar{p}_i\dot{\alpha}_k + F_k\bar{\vec{u}}_i.$$

The modelling of these interfacial quantities remains a difficult issue of multiphase flows. To obtain a solution of this system of equations, it is necessary to provide expressions that can be considered as interfacial closure relationships. These relationships depend heavily on the kind of multiphase flow and on its topology. They are now explained in the context of interface and detonation applications.

Modelling of the average interfacial pressure $\bar{p}_i$ and velocity $\bar{\vec{u}}_i$. In the work of Baer and Nunziato [3] and Kapila et al. [21] $\bar{p}_i$ is taken equal to the pressure of the most compressible phase, while $\bar{\vec{u}}_i$ is taken equal to the velocity of the less compressible phase. In Saurel and Abgrall [32], $\bar{p}_i$ is taken equal to the mixture pressure and $\bar{\vec{u}}_i$ to the velocity of the center of mass. In the present paper, thanks to the new homogenization method (DEM), we obtain explicit formulas for $\bar{p}_i$ and $\bar{\vec{u}}_i$ that are symmetric, compatible with the second law of thermodynamics, and responsible for the fulfilment of interface conditions when dealing with contact/interface problems.

Modelling of $\dot{\alpha}_k = -\langle\delta\bar{\vec{u}}_i\nabla X_k\rangle$. Baer and Nunziato [3] were the first to propose to model the rate of change in volume fraction as proportional to the phase pressure differential: $\dot{\alpha}_k = \mu\Delta p_k$. The parameter μ

controls the rate at which pressure equilibrium is reached. Saurel and Abgrall [32], Kapila et al. [22] and Saurel and Le Metayer [34] by different considerations propose to take this factor equal to infinity. In the present paper, we provide general explicit formula for μ and demonstrate that this coefficient tends to infinity in the context of detonation applications.

Modelling of $F_k = \langle \delta p_i \nabla X_k \rangle$. The latter authors have proposed and justified on physical backgrounds to model the pressure drag force as proportional to the phase velocity differential: $F_k = \lambda \Delta \vec{u}_k$, where λ is a relaxation parameter that tends to infinity in the context of interface problems and detonations in condensed energetic materials. In the present paper, we derive explicit formula for this relaxation parameter. We also show that it is connected to the parameter μ. In the field of detonation applications, it is demonstrated that it tends to infinity too.

Modelling of the mass transfer $\dot{m}_k = \langle \rho(\vec{u} - \vec{\sigma}) \nabla X \rangle_k$. The mass production term $\dot{\omega}_{k,m}$ of mth species, component of the kth phase obeys general laws for chemical reactive systems. Difficulties appear when the different $\dot{m}_k$ have to be modelled. This mass transfer represents the general production term of phase k through interfaces with other phases. Knowledge of the physics is required to express this term that can be very different according to the phenomenon considered: there are no difficulties to figure out that the mechanisms involved in the vaporization of a liquid are different of those involved in the combustion of a solid material. For our purposes, most of the laws that give the depletion rate of a solid explosive are based on Arrhenius laws or Vieille's law, depending on temperatures or pressures of the different phases. Nevertheless, there is no general restriction to model this term except that relation $\sum_{k=1,\ldots,N} \dot{m}_k = 0$ must be verified, which is the condition expressing the conservation of total mass in the multiphase mixture and that the chemical kinetics verify the permanence of atomic substances.

2.1. The general model

For conveniences, we note $p_i = \bar{p}_i$, $\vec{u}_i = \bar{\vec{u}}_i$.

The general continuous model (2.3) can be rewritten as (2.4) by expressing all the closure relations:

$$\begin{cases} \dfrac{\partial \alpha_k}{\partial t} + \vec{u}_i \nabla \alpha_k = \dot{\alpha}_k + \dfrac{\dot{m}_k}{\rho_{\mathrm{IR}}}, \\ \dfrac{\partial (\alpha\rho)_k}{\partial t} + \operatorname{div}(\alpha\rho\vec{u})_k = \dot{m}_k, \\ \dfrac{\partial (\alpha\rho\vec{u})_k}{\partial t} + \operatorname{div}(\alpha\rho\vec{u} \otimes \vec{u})_k + \nabla(\alpha p)_k = p_i \nabla \alpha_k + \vec{F}_k + \dot{m}_k \vec{u}_i, \\ \dfrac{\partial (\alpha\rho E)_k}{\partial t} + \operatorname{div}(\alpha(\rho E + p)\vec{u})_k = (p\vec{u})_i \nabla \alpha_k + \vec{u}_i \vec{F}_k - p_i \dot{\alpha}_k + \dot{m}_k E_{\mathrm{IR}}, \\ \dfrac{\partial (\alpha\rho Y_m)_k}{\partial t} + \operatorname{div}(\alpha\rho Y_m \vec{u})_k = \dot{m}_{mk}. \end{cases} \tag{2.4}$$

The variables with subscript IR appear only when interfaces are reactive, that is when mass transfer occurs. Determination of these variables will be discussed latter.

The multiphase equations have two formulations (2.3) and (2.4), which are the same. In the following, the two formulations will be used indifferently. But the closure issue corresponding to the determination of p_i, $\vec{u}_i$, μ and λ as well as the numerical approximation of these equations necessitates a new homogeneization method that is developed in Section 3.

3. Building of a two-dimensional discrete multiphase model

The new approach based of Abgrall and Saurel [2] is extended to the simulation of detonation waves. The method considers the numerical cell C_{ij} as a representative physical multiphase control volume. The pure fluid

equations are discretized at the grain/microscopic scale. Then these equations are averaged. A set of algebraic relations for the flow unknowns are obtained. In the following, the development of this method is detailed.

We wish to model a dispersed two-phase flow as depicted in Fig. 2(a). It is a media composed of grains of a reactive granular material (phase 1) into a gaseous phase (phase 2). The latter comes from the chemical decomposition of the explosive or can be initially trapped into pores.

The model relies on the topology of this two-phase media. A macroscopic two-phase volume contains two phases, which contains n grains of phase 1 per volume unit. The size of a microscopic volume is below the size of the individual grain. It may only contain a fraction of the interface grain–gas (cf. Fig. 2(b)). At this microscopic scale, the interactions between the two fluids are given by the solutions of Riemann problems between non-miscible fluids governed by the Euler equations. The macroscopic equations are obtained by making the inventory of all the contacts, examining the surfaces of these contacts and summing solution of all these interface problems.

The mesh is composed of numerical cells $C_{ij} =]x_{i-1/2}, x_{i+1/2}[\times]y_{i-1/2}, y_{i+1/2}[$ of uniform length Δx and of uniform height Δy. These control volumes are supposed to be larger than the elementary volume of the two-phase media. Δt is the time step of the temporal integration.

In order to obtain the two-phase flow model in an Eulerian frame, the mesh and the two-phase flow are superimposed. The two-phase mixture evolution is examined in the control volume C_{ij} (cf. Fig. 3(a)) during the time step Δt.

In the sake of clarity, no mass transfer is considered. For the calculations clarity and because the solution of Riemann problem is known in only one space dimension, grains are considered to be cubic rather than spherical. The development is made in two dimensions, the extension to three dimensions being straightforward. The volume fraction is a surface fraction: $\alpha_1 = na^2$, a is the length of the side of the grain. In each control volume (mesh cell), the different flow variables of the phases are constant in the cells. This approximation is usual in Godunov-type numerical schemes.

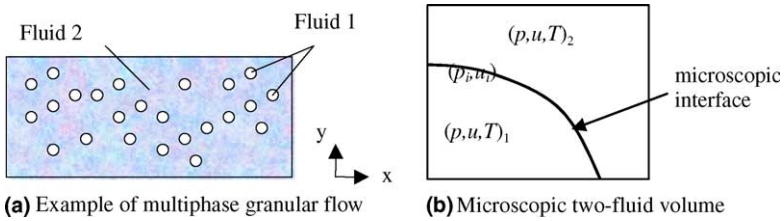

Fig. 2. Schematic representation of the two-phase control volume and interface control volume.

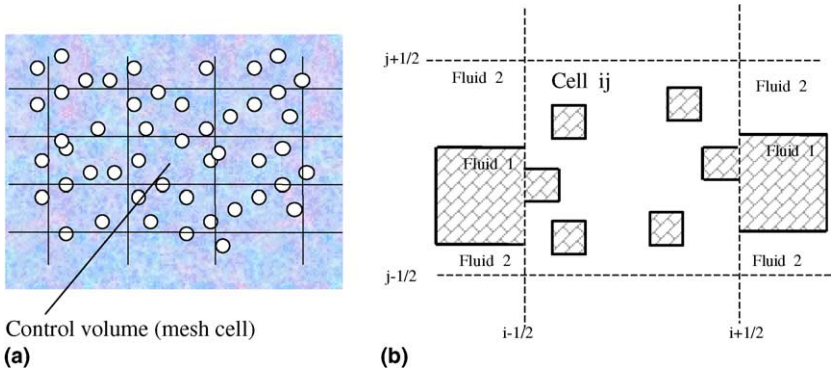

Fig. 3. (a) Superimposition of the mesh and two-phase flow. (b) Magnified view of control volume C_{ij}, phase 1 being in grey.

In this flow representation, α_1 and n are piecewise constant functions. Thus the size of a grain – characteristic length – is also a piecewise constant function. This leads to the representation depicted in Fig. 3(b).

In the following, the pure fluid instantaneous equations are recalled. We define volume, surface and temporal averaging operators that will be needed in the building of the multiphase equations. We also define the contact surfaces between phases inside the cells and at its boundary. This enables the evaluation of the fluxes coming from the averaging process.

3.1. Local instantaneous pure fluid equations

At the microscopic scale, each phase obeys the Euler reactive equations that reads from system (2.1):

$$\frac{\partial W}{\partial t}+\frac{\partial F}{\partial x}+\frac{\partial G}{\partial y}=0, \tag{3.1}$$

$$W=(1,\rho,\rho u,\rho v,\rho E,\rho Y_m),\quad F=(0,\rho u,\rho u^2+p,\rho uv,\rho(E+p)u,\rho uY_m),$$
$$G=(0,\rho v,\rho uv,\rho v^2+p,(\rho E+p)v,\rho vY_m).$$

The first equation $\frac{\partial 1}{\partial t}+\frac{\partial 0}{\partial x}+\frac{\partial 0}{\partial y}=0$ is a trivial identity that simplifies the presentation of the volume fraction equation. We denote $\vec{\sigma}=(\sigma_x,\sigma_y)$. Thus system (3.1) is augmented by Eq. (2.2)

$$\frac{\partial X_k}{\partial t}+\sigma_x\frac{\partial X_k}{\partial x}+\sigma_y\frac{\partial X_k}{\partial y}=0$$

that is used to select the fluids. After some algebraic manipulations, the evolution of the unknowns for each phase k in each cell C_{ij}, during the time step Δt is given by:

$$\int_0^{\Delta t}\int_{C_{ij}}\left(\frac{\partial(X_kW)}{\partial t}+\frac{\partial(X_kF)}{\partial x}+\frac{\partial(X_kG)}{\partial y}\right)\mathrm{d}x\,\mathrm{d}y\,\mathrm{d}t=\int_0^{\Delta t}\int_{C_{ij}}\left((F-\sigma_xW)\frac{\partial X_k}{\partial x}+(G-\sigma_yW)\frac{\partial X_k}{\partial y}\right)\mathrm{d}x\,\mathrm{d}y\,\mathrm{d}t. \tag{3.2}$$

With the previous notations and with the help of the trivial identity, the evolution of the characteristic function is recovered. Thus (3.2) summarizes (2.2) and (3.1) in each fluid.

The terms in the right-hand side of this equation represent the Lagrangian fluxes. In the vicinity of an interface between two fluids, the interface conditions hold: uniform pressure and velocity. Thus $F-\sigma_xW=(-u,0,p,0,pu,0)$ and $G-\sigma_yW=(-v,0,0,p,pv,0)$ are constant at the vicinity of a two-fluid interface ($\nabla X_k\neq 0$). We note in the following:

$$F^{\mathrm{lag}}=F-\sigma_xW\quad\text{and}\quad G^{\mathrm{lag}}=G-\sigma_yW. \tag{3.3}$$

We now turn to the evaluation of the different terms of (3.2). The average multiphase discrete equations will follow.

3.2. Average discrete equations

Each cell of the mesh contains initially two phases. The details of the derivation are made explicit for the phase 1 only. The equations of the second phase can be obtained by changing the subscripts adequately. The evolutionary equations of the phase 1 are:

$$\int_0^{\Delta t}\int_{C_{ij}}\left(\frac{\partial(X_1W)}{\partial t}+\frac{\partial(X_1F)}{\partial x}+\frac{\partial(X_1G)}{\partial y}\right)\mathrm{d}x\,\mathrm{d}y\,\mathrm{d}t=\int_0^{\Delta t}\int_{C_{ij}}\left(F^{\mathrm{lag}}\frac{\partial X_1}{\partial x}+G^{\mathrm{lag}}\frac{\partial X_1}{\partial y}\right)\mathrm{d}x\,\mathrm{d}y\,\mathrm{d}t. \tag{3.8}$$

Five integrals have to be evaluated $I_1 + I_2 + I_3 = I_4 + I_5$

$$I_1 = \int_0^{\Delta t} \int_{C_{ij}} \frac{\partial (X_1 W)}{\partial t} \, \mathrm{d}x \, \mathrm{d}y \, \mathrm{d}t \quad \text{temporal term,} \tag{3.9}$$

$$I_2 = \int_0^{\Delta t} \int_{C_{ij}} \frac{\partial (X_1 F)}{\partial x} \, \mathrm{d}x \, \mathrm{d}y \, \mathrm{d}t \quad \text{horizontal convective flux,} \tag{3.10}$$

$$I_3 = \int_0^{\Delta t} \int_{C_{ij}} \frac{\partial (X_1 G)}{\partial y} \, \mathrm{d}x \, \mathrm{d}y \, \mathrm{d}t \quad \text{vertical convective flux,} \tag{3.11}$$

$$I_4 = \int_0^{\Delta t} \int_{C_{ij}} F^{\mathrm{lag}} \frac{\partial X_1}{\partial y} \, \mathrm{d}x \, \mathrm{d}y \, \mathrm{d}t \quad \text{Lagrangian horizontal flux,} \tag{3.12}$$

$$I_5 = \int_0^{\Delta t} \int_{C_{ij}} G^{\mathrm{lag}} \frac{\partial X_1}{\partial y} \, \mathrm{d}x \, \mathrm{d}y \, \mathrm{d}t \quad \text{Lagrangian vertical flux.} \tag{3.13}$$

To this end, let us define the following averaging operators.

- *Volume average*

$$\langle f \rangle = \frac{1}{C_{ij}} \int_{C_{ij}} f \, \mathrm{d}V. \tag{3.4}$$

- *Temporal average*

$$\tilde{f} = \frac{1}{\Delta t} \int_{\Delta t} f \, \mathrm{d}t. \tag{3.5}$$

- *Surface averages*

$$\bar{f} = \frac{1}{\Delta y} \int_{y_{j-1/2}}^{y_{j+1/2}} f \, \mathrm{d}y \quad \text{and} \quad \hat{f} = \frac{1}{\Delta x} \int_{x_{i-1/2}}^{x_{i+1/2}} f \, \mathrm{d}x. \tag{3.6}$$

- *Internal average*

$$\langle\langle f \rangle\rangle = \frac{\langle Xf \rangle}{\langle X \rangle} = \frac{\langle Xf \rangle}{\alpha}. \tag{3.7}$$

We have $\langle f \rangle = \hat{\tilde{f}} = \bar{\hat{f}}$.

3.3. Approximation of the temporal term I_1

$$I_1 = \int_0^{\Delta t} \int_{C_{ij}} \frac{\partial (X_1 W_1)}{\partial t} \, \mathrm{d}x \, \mathrm{d}y \, \mathrm{d}t = \int_{C_{ij}} \int_0^{\Delta t} \frac{\partial (X_1 W_1)}{\partial t} \, \mathrm{d}x \, \mathrm{d}y \, \mathrm{d}t = \int_{C_{ij}} \left((X_1 W_1)_{ij}^{n+1} - (X_1 W_1)_{ij}^{n} \right) \mathrm{d}x \, \mathrm{d}y,$$

that is,

$$I_1 = \Delta x \Delta y \left((\alpha \langle\langle W \rangle\rangle)_{1,ij}^{n+1} - (\alpha \langle\langle W \rangle\rangle)_{1,ij}^{n} \right). \tag{3.14}$$

3.4. Approximation of the horizontal convective flux I_2

$$I_2 = \int_0^{\Delta t} \int_{C_{ij}} \frac{\partial (XF)_1}{\partial x} \, \mathrm{d}x \, \mathrm{d}y \, \mathrm{d}t = \int_0^{\Delta t} \int_{y_{j-1/2}}^{y_{j+1/2}} \int_{x_{i-1/2}}^{x_{i+1/2}} \frac{\partial (XF)_1}{\partial x} \, \mathrm{d}x \, \mathrm{d}y \, \mathrm{d}t$$
$$= \int_0^{\Delta t} \int_{y_{j-1/2}}^{y_{j+1/2}} \left((XF)_{1,i+1/2} - (XF)_{1,i-1/2} \right) \mathrm{d}y \, \mathrm{d}t. \tag{3.15}$$

The surface average at the abscissa $i - 1/2$ is:

$$\Delta y \overline{XF}_{1,i-1/2} = \int_{y_{j-1/2}}^{y_{j+1/2}} (XF)_{1,i-1/2} \, \mathrm{d}y.$$

The case of one isolated grain of Fig. 3(b) is considered at the cell boundary as represented in Figs. 4(a) and (b). Such configuration appears because the flow variables, in particular the characteristic length of a grain, are piecewise constant functions. The case of several grains can be treated in the same way.

The cell boundary, delimitated by the segment $]y_{j-1/2}; y_{j+1/2}[$, can be decomposed in several segments associated with different kinds of contact l (Fig. 4(a)). Each type of contact $l = (p, q)$ means that p is the

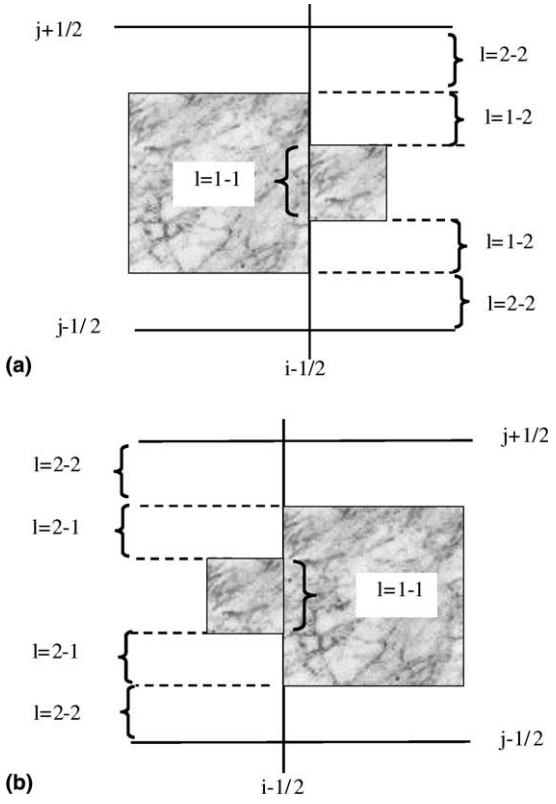

Fig. 4. (a) Schematic representation of the different contacts l at a cell boundary when fluid 1 volume fraction gradient is negative. (b) Schematic representation of the different contacts l when the grain size increases discontinuously.

fluid at the left boundary and the fluid q at the right boundary. In the case of Fig. 4(a), there are three types of contact $l = 1$–1, $l = 1$–2, $l = 2$–2. The height of contact l is denoted $S_l = S_{pq}$ and will be determined latter. The integral can be decomposed in a sum of elementary integrals:

$$\Delta y\overline{XF}_{1,i-1/2} = \sum_l \int_0^{S_l} (XF)_{1,i-1/2}(l)\,\mathrm{d}y.$$

In the following, there is no differences between the height of contact and the surface of contact as the model is presented in a 2D configuration. Each elementary integral is evaluated in the following way:

$$\int_0^{S_l} (XF)_{1,i-1/2}(l)\,\mathrm{d}y \equiv S_l X^*_{1,i-1/2}(l)\cdot F^*_{1,i-1/2}(l) = S_{pq}X^*_{1,i-1/2}(p,q)F^*_{1,i-1/2}(p,q).$$

The initial states of the fluids p and q, respectively, on the left and on the right of the boundary $i-1/2$ will generate pressure waves for which the solution is given by a Riemann solver. Some examples of Riemann solvers can be found in the literature. This solution provides the value of the flux $F^*_{1,i-1/2}(p,q)$. $X^*_{1,i-1/2}(p,q)$ is the value of the characteristic function of phase 1 at the boundary $i-1/2$. When fluid 1 is in contact with fluid 1, this function is equal to 1. Its value is 0 inside the fluid 2. When fluid 1 is in contact with fluid 2, its value depends on the interface velocity $u^*_{1,i-1/2}(1,2)$. When it is positive, the function $X^*_{1,i-1/2}(p,q)$ is equal to 1 and 0 in the opposite case. When the interface velocity is positive it means that fluid 1 is coming into the control volume. This interface velocity is also solution of the Riemann solver.

There is still to model the contact height length $S_l = S_{pq}$. In the case depicted in Fig. 4(a), S_{11} can be evaluated by: $S_{11} = \Delta y\alpha_{1,i}$. Indeed, the height of contact between fluid 1 at the left of the boundary and fluid 1 at the right of the boundary is the smallest surface present at the boundary. In Fig. 4(a), the smallest surface is the right one. We model the surface fraction by the volume fraction. The height of contact between fluid 1 and fluid 2 is equal to the difference of the two levels $S_{12} = \Delta y(\alpha_{1,i-1j} - \alpha_{1,ij})$. Consequently $S_{22} = \Delta y\alpha_{2,i-1j}$.

Thus the average flux at the boundary $i-1/2$ is:

$$\Delta y\overline{XF}_{1,i-1/2} = \sum_{p,q=1,2} S_{pq}X^*_{1,i-1/2}(p,q)F^*_{1,i-1/2}(p,q).$$

We can proceed in the same way for the case depicted in Fig. 4(b) when the grain size increases discontinuously.

In the case depicted in Fig. 4(b), the contacts are different. We must consider the contact 1–2 that does not exist in the case depicted in Fig. 4(a). Moreover, the heights of contact between fluids are different from Fig. 4(a) case. Here, we have $S_{11} = \Delta y\alpha_{1,i-1j}$. The other heights of contact are $S_{22} = \Delta y\alpha_{2,i-1j}$ and $S_{21} = \Delta y(\alpha_{1,ij} - \alpha_{1,i-1j})$. The values of $X^*_{1,i-1/2}(p,q)$ and $F^*_{1,i-1/2}(p,q)$ are deduced from a Riemann solver between fluids p and q which are here and there of $i-1/2$.

Table 1 summarises the different cases and gives formulas valid for both situations depicted in Figs. 4(a) and (b).

Thus, the average surface horizontal convective flux at the cell boundary $i-1/2$ is:

$$\begin{aligned}\Delta y\overline{XF}_{1,i-1/2} &= \int_{y_{j-1/2}}^{y_{j+1/2}} (XF)_{1,i-1/2}\,\mathrm{d}y \\ &= \Big(S_{11}X^*_{1,i-1/2}(1,1)F^*_{i-1/2}(1,1) + S_{12}X^*_{1,i-1/2}(1,2)F^*_{i-1/2}(1,2) + S_{21}X^*_{1,i-1/2}(2,1)F^*_{i-1/2}(2,1)\Big).\end{aligned}$$

We can proceed in the same way for the evaluation of the convective flux at the boundary $i+1/2$. I_2 then becomes

Table 1
Evaluation of the different horizontal convective fluxes at the cell boundary $i-1/2$

Type of contact	Surface of contact	Indicator function 1	Convective flux
1–1	$S_{11}=\Delta y\min(\alpha_{1,i-1j},\alpha_{1,ij})$	$X_1^*(1,1)=1$	$F^*(1,1)$
1–2	$S_{12}=\Delta y\max(\alpha_{1,i-1j}-\alpha_{1,ij},0)$	$X_1^*(1,2)=\begin{cases}1 & \text{if } u^*(1,2)>0\\ 0 & \text{otherwise}\end{cases}$	$F^*(1,2)$
2–1	$S_{21}=\Delta y\max(\alpha_{1,ij}-\alpha_{1,i-1j},0)$	$X_1^*(2,1)=\begin{cases}1 & \text{if } u^*(2,1)<0\\ 0 & \text{otherwise}\end{cases}$	$F^*(2,1)$
2–2	$S_{22}=\Delta y\min(\alpha_{2,i-1j},\alpha_{2,ij})$	$X_1^*(2,2)=0$	$F^*(2,2)$

$$I_2=\int_0^{\Delta t}\int_{y_{j-1/2}}^{y_{j+1/2}}((XF)_{1,i+1/2}-(XF)_{1,i-1/2})\,\mathrm{d}y\,\mathrm{d}t=\Delta y\int_0^{\Delta t}((\overline{XF})_{1,i+1/2}-(\overline{XF})_{1,i-1/2})\,\mathrm{d}t$$
$$=\Delta y\Delta t\left((\tilde{\tilde{XF}})_{1,i+1/2}-(\tilde{\tilde{XF}})_{1,i-1/2}\right).$$

For a time step small enough $\tilde{\tilde{XF}}=\overline{XF}$ at each boundaries $i-1/2$ and $i+1/2$ and the preceding equation becomes

$$I_2=\Delta y\Delta t\left((\overline{XF})_{1,i+1/2}-(\overline{XF})_{1,i-1/2}\right). \tag{3.16}$$

3.5. Approximation of horizontal Lagrangian flux I_4

The horizontal Lagrangian integral is

$$I_4=\int_0^{\Delta t}\int_{C_{ij}}F^{\mathrm{lag}}\frac{\partial X_1}{\partial x}\,\mathrm{d}x\,\mathrm{d}y\,\mathrm{d}t. \tag{3.17}$$

The latter can be decomposed into two parts

$$I_4=\int_0^{\Delta t}\left(\underbrace{\int_{y_{j-1/2}}^{y_{j+1/2}}F^{\mathrm{lag}}_{i-1/2}[X_1]_{i-1/2}\,\mathrm{d}y+\int_{y_{j-1/2}}^{y_{j+1/2}}F^{\mathrm{lag}}_{i+1/2}[X_1]_{i+1/2}\,\mathrm{d}y}_{I_{4,\mathrm{boundary}}}+\underbrace{\int_{y_{j-1/2}}^{y_{j+1/2}}F^{\mathrm{lag}}_{\mathrm{internal}}[X_1]_{\mathrm{internal}}\,\mathrm{d}y}_{I_{4,\mathrm{internal}}}\right)\mathrm{d}t, \tag{3.18}$$

$I_{4,\mathrm{boundary}}$ corresponds to the Lagrangian flux that comes from the interfaces present at the cell boundary of the control volume C_{ij}. $I_{4,\mathrm{internal}}$ corresponds to the Lagrangian flux that comes from the interfaces present into the control volume C_{ij}. We evaluate $I_{4,\mathrm{boundary}}$ then $I_{4,\mathrm{internal}}$. The contact surfaces between the pure fluids that must be taken into account are the same as for the evaluation of the convective fluxes. Then

$$\Delta y\overline{F^{\mathrm{lag}}_{i-1/2}[X_1]_{i-1/2}}=\sum_{p,q=1,2}\int_0^{S_{pq}}F^{\mathrm{lag}}_{i-1/2}[X_1]_{i-1/2}\,\mathrm{d}y.$$

Each elementary integral can be obtained in the following way:

$$\int_0^{S_{pq}}F^{\mathrm{lag}}_{i-1/2}[X_1]_{i-1/2}\,\mathrm{d}y\equiv S_{pq}F^{\mathrm{lag},*}_{i-1/2}(p,q)[X_1^*]_{i-1/2}(p,q).$$

The four possible configurations ($p, q = 1, 2$) are summarized in Table 2. The jump of the indicator function $[X_1^*]$ depends on the sign of the interface velocity, given by the solution of the Riemann problem. In the configuration $(1, 2)$ – fluid 1 and fluid 2 are, respectively, at the left and right of the boundary. $[X_1^*]$ is equal to -1 if the velocity is positive. Indeed, X_1 is equal to 1 in the fluid 1 and X_1 is equal to 0 in fluid 2. Thus the jump is equal to -1 if fluid 1 enters the numerical cell. If the interface velocity is negative, fluid 1 exits the numerical cell thus the jump is zero. For the configuration $(1, 1)$, the jump is always zero because there is no interface. Consequently, we get:

$$\begin{aligned}\Delta y\overline{F^{\text{lag}}[X_1]}_{i-1/2} &= \int_{y_{j-1/2}}^{y_{j+1/2}} \left(F^{\text{lag}}[X_1]\right)_{i-1/2} \mathrm{d}y\,\mathrm{d}t \\ &= \left(S_{12}[X_1^*]_{i-1/2}(1,2)F^{\text{lag},*}_{i-1/2}(1,2) + S_{21}[X_1^*]_{i-1/2}(2,1)F^{\text{lag},*}_{i-1/2}(2,1)\right). \end{aligned} \tag{3.19}$$

We proceed in the same way for the evaluation of the horizontal Lagrangian flux at the cell boundary $i + 1/2$.

We remark that the jump of the indicator function is non-zero ($[X_1]^*_{i-1/2} \neq 0$ and $[X_1]^*_{i+1/2} \neq 0$) on the segments that are the thick lines in Fig. 5.

The term $I_{4,\text{internal}}$ related to the interfaces present inside the two-phase control volume is now evaluated. The interfaces that are considered are represented in Fig. 6.

The flux $I_{4,\text{internal}}$ is given by

$$I_{4,\text{internal}} = \int_0^{\Delta t} \int_{y_{j-1/2}}^{y_{j+1/2}} F^{\text{lag}}_{\text{internal}}[X_1]_{\text{internal}} \,\mathrm{d}y\,\mathrm{d}t == \int_0^{\Delta t} \sum_{\text{internal interfaces}} \int_0^a F^{\text{lag}}_{\text{internal}}[X_1]_{\text{internal}} \,\mathrm{d}y\,\mathrm{d}t.$$

We group the interfaces by two, that correspond to the contacts (2–1) and (1–2) as shown in Fig. 6. As $[X_1]_{\text{internal}}(2, 1) = -1$ and $[X_1]_{\text{internal}}(1, 2) = +1$, we get:

$$I_{4,\text{internal}} = \int_0^{\Delta t} \sum_{\text{number of internal grains}} \int_0^a \left(F^{\text{lag},*}_{ij}(2,1) - F^{\text{lag},*}_{ij}(1,2)\right) \mathrm{d}y\,\mathrm{d}t.$$

We note $\bar{F} = \frac{1}{a}\int_0^a F\,\mathrm{d}y$, then:

$$I_{4,\text{internal}} = \int_0^{\Delta t} Na \int_0^a \left(F^{\text{lag},*}_{ij}(2,1) - F^{\text{lag},*}_{ij}(1,2)\right) \mathrm{d}y\,\mathrm{d}t,$$

where $N = n\Delta x\Delta y$. Thus,

Table 2
Evaluation of the horizontal Lagrangian fluxes for the various configurations at $i - 1/2$

Type of contact	Surface of contact	Jump of the indicator function 1	Lagrangian flux
1–1	$S_{11} = \Delta y \min(\alpha_{1,i-1j}, \alpha_{1,ij})$	$[X_1^*](1,1) = 0$	$F^{\text{lag},*}(1,1)$
1–2	$S_{12} = \Delta y \max(\alpha_{1,i-1j} - \alpha_{1,ij}, 0)$	$[X_1^*](1,2) = \begin{cases} -1 & \text{if } u_1^*(1,2) > 0 \\ 0 & \text{otherwise} \end{cases}$	$F^{\text{lag},*}(1,2)$
2–1	$S_{21} = \Delta y \max(\alpha_{1,ij} - \alpha_{1,i-1j}, 0)$	$[X_1^*](2,1) = \begin{cases} 1 & \text{if } u_1^*(2,1) > 0 \\ 0 & \text{otherwise} \end{cases}$	$F^{\text{lag},*}(2,1)$
2–2	$S_{22} = \Delta y \min(\alpha_{2,ij-1}, \alpha_{2,ij})$	$[X_1^*](2,2) = 0$	$F^{\text{lag},*}(2,2)$

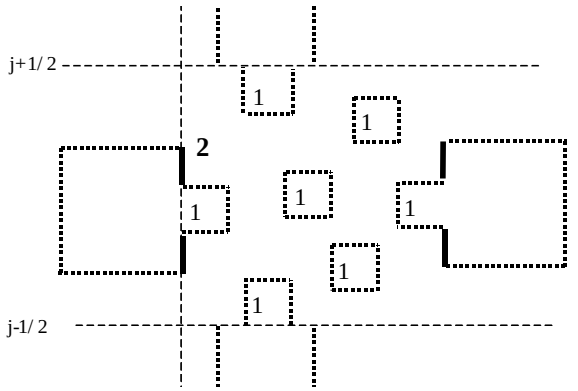

Fig. 5. Thick lines represent the interfaces at the cell boundaries of the control volume that produce Lagrangian fluxes.

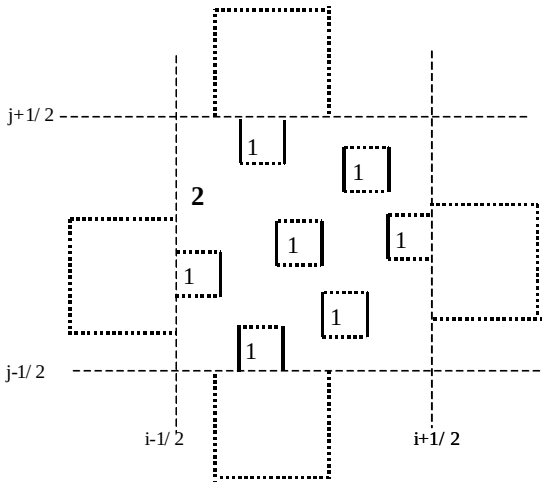

Fig. 6. Representation of the interfaces that are involved in the evaluation of the internal non-conservative products in the horizontal direction. The dotted lines (horizontal interfaces) are not involved in the calculation.

$$I_{4,\text{internal}} = Na\int_0^{\Delta t}\left(\overline{F_{ij}^{\text{lag},*}}(2,1) - \overline{F_{ij}^{\text{lag},*}}(1,2)\right)\mathrm{d}t = Na\left(\overline{\tilde{F}_{ij}^{\text{lag},*}}(2,1) - \overline{\tilde{F}_{ij}^{\text{lag},*}}(1,2)\right).$$

For a time step small enough, $\tilde{\bar{F}} = \bar{F}$. Because the states are constant here and there the interface, $\bar{F} = F$. Thus,

$$I_{4,\text{internal}} = \Delta t Na\left(F^{\text{lag},*}(2,1) - F^{\text{lag},*}(1,2)\right)_{ij}. \tag{3.20}$$

Finally

$$I_4 = I_{4,\text{boundary}} + I_{4,\text{internal}}, \tag{3.21}$$

$$I_4 = \Delta y\Delta t\left(\overline{F^{\text{lag},*}[X_1^*]}_{i-1/2} + \overline{F^{\text{lag},*}[X_1^*]}_{i+1/2}\right) + \Delta t Na\left(F^{\text{lag},*}(2,1) - F^{\text{lag},*}(1,2)\right)_{ij}. \tag{3.22}$$

The approximation of the convective vertical I_3 as well as the vertical Lagrangian flux I_5 are done in the same way as I_2 and I_4, respectively.

3.6. Summary of the discrete averaged equations

The discretization of the averaged equations for multiphase flows according to the geometrical representation of Fig. 3 is given by:

$$\begin{aligned}
&\frac{(\alpha\langle W\rangle)_{1,ij}^{n+1}-(\alpha\langle W\rangle)_{1,ij}^{n}}{\Delta t}+\frac{(\overline{XF})_{1,i+1/2}-(\overline{XF})_{1,i-1/2}}{\Delta x}+\frac{(\widehat{XG})_{1,j+1/2}-(\widehat{XG})_{1,j-1/2}}{\Delta y}\\
&\quad=\frac{\overline{F^{\mathrm{lag}}[X_1]}_{i+1/2}+\overline{F^{\mathrm{lag}}[X_1]}_{i-1/2}}{\Delta x}+\frac{\widehat{G^{\mathrm{lag}}[X_1]}_{j+1/2}+\widehat{G^{\mathrm{lag}}[X_1]}_{j-1/2}}{\Delta y}+\frac{N}{\Delta x\Delta y}a\Big(\overline{F^{\mathrm{lag}}}(2,1)\\
&\qquad-\overline{F^{\mathrm{lag}}}(1,2)\Big)_{ij}+\frac{N}{\Delta x\Delta y}a\Big(\widehat{G^{\mathrm{lag}}}(2,1)-\widehat{G^{\mathrm{lag}}}(1,2)\Big)_{ij}
\end{aligned}\tag{3.23}$$

The horizontal convective fluxes are given by:

$$\begin{aligned}
\overline{XF}_{1,i+1/2}&=\max(0;\alpha_{1,ij}-\alpha_{1,i+1j})X^{*}_{1,i+1/2}(1,2)F^{*}_{i+1/2}(1,2)+\min(\alpha_{1,i+1j};\alpha_{1,ij})X^{*}_{1,i+1/2}(1,1)F^{*}_{i+1/2}(1,1)\\
&\quad+\max(0;\alpha_{1,i+1j}-\alpha_{1,ij})X^{*}_{1,i+1/2}(2,1)F^{*}_{i+1/2}(2,1),
\end{aligned}$$

$$\begin{aligned}
\overline{XF}_{1,i-1/2}&=\max(0;\alpha_{1,i-1j}-\alpha_{1,ij})X^{*}_{1,i-1/2}(1,2)F^{*}_{i-1/2}(1,2)+\min(\alpha_{1,ij};\alpha_{1,i-1j})X^{*}_{1,i-1/2}(1,1)F^{*}_{i-1/2}(1,1)\\
&\quad+\max(0;\alpha_{1,ij}-\alpha_{1,i-1j})X^{*}_{1,i-1/2}(2,1)F^{*}_{i-1/2}(2,1).
\end{aligned}$$

The vertical convective fluxes are given by:

$$\begin{aligned}
\widehat{XG}_{1,j+1/2}&=\max(0;\alpha_{1,ij}-\alpha_{1,ij+1})X^{*}_{1,j+1/2}(1,2)G^{*}_{j+1/2}(1,2)+\min(\alpha_{1,ij+1};\alpha_{1,ij})X^{*}_{1,j+1/2}(1,1)G^{*}_{j+1/2}(1,1)\\
&\quad+\max(0;\alpha_{1,ij+1}-\alpha_{1,ij})X^{*}_{1,j+1/2}(2,1)G^{*}_{j+1/2}(2,1),
\end{aligned}$$

$$\begin{aligned}
\widehat{XG}_{1,j-1/2}&=\max(0;\alpha_{1,ij-1}-\alpha_{1,ij})X^{*}_{1,j-1/2}(1,2)G^{*}_{j-1/2}(1,2)+\min(\alpha_{1,ij};\alpha_{1,i-1j})X^{*}_{1,j-1/2}(1,1)G^{*}_{j-1/2}(1,1)\\
&\quad+\max(0;\alpha_{1,ij}-\alpha_{1,ij-1})X^{*}_{1,j-1/2}(2,1)G^{*}_{j-1/2}(2,1).
\end{aligned}$$

The horizontal Lagrangian fluxes are given by:

$$\begin{aligned}
\overline{F^{\mathrm{lag}}[X_1]}_{i+1/2}=&\ \max(0;\alpha_{1,ij}-\alpha_{1,i+1j})[X_1]^{*}_{i+1/2}(1,2)F^{\mathrm{lag}*}_{i+1/2}(1,2)\\
&+\max(0;\alpha_{1,i+1j}-\alpha_{1,ij})[X_1]^{*}_{i+1/2}(2,1)F^{*}_{i+1/2}(2,1),
\end{aligned}$$

$$\begin{aligned}
\overline{F^{\mathrm{lag}}[X_1]}_{1,i-1/2}=&\ \max(0;\alpha_{1,i-1j}-\alpha_{1,ij})[X_1]^{*}_{i-1/2}(1,2)F^{\mathrm{lag},*}_{i-1/2}(1,2)\\
&+\max(0;\alpha_{1,ij}-\alpha_{1,i-1j})[X_1]^{*}_{i-1/2}(2,1)F^{\mathrm{lag},*}_{i-1/2}(2,1).
\end{aligned}$$

The vertical Lagrangian fluxes read:

$$\begin{aligned}
\widehat{G^{\mathrm{lag}}[X_1]}_{j+1/2}=&\ \max(0;\alpha_{1,ij}-\alpha_{1,ij+1})[X_1]^{*}_{j+1/2}(1,2)G^{\mathrm{lag},*}_{j+1/2}(1,2)\\
&+\max(0;\alpha_{1,ij+1}-\alpha_{1,ij})[X_1]^{*}_{j+1/2}(2,1)G^{\mathrm{lag},*}_{j+1/2}(2,1),
\end{aligned}$$

$$\widehat{G^{\mathrm{lag}}[X_1]}_{j-1/2} = \max(0;\alpha_{1,ij-1}-\alpha_{1,ij})[X_1]^*_{j-1/2}(1,2)G^{\mathrm{lag},*}_{1,j-1/2}(1,2) + \max(0;\alpha_{1,ij}-\alpha_{1,ij-1})[X_1]^*_{j-1/2}(2,1)G^{\mathrm{lag},*}_{1,j-1/2}(2,1).$$

In these formulas (p,q) represents the configuration where fluid p is at the left (or bottom) of the boundary and fluid q on the right (or top) of the boundary.

This discrete formulation (3.23) is difficult to analyse for physical interpretation. In the following paragraph, the continuous limit of these equations is derived and analysed. These discrete equations represent the numerical scheme that will be used in the numerical simulations.

4. Continuous limit of the discrete equations

The aim of this section is to derive the continuous analogue of system (3.23) as a system of partial differential equations. It will be shown that the discrete equations contain implicitly the relaxation terms as well as the expressions for the averaged interfacial pressure and velocity. Knowledge of the continuous limit is helpful for a better understanding of the model structure and properties. The continuous limit of the discrete equations consists in determining the system of PDE that results from Eq. (3.23) when Δt, Δx and Δy tend to zero. This system of PDE is always hyperbolic and satisfies a dissipative inequality. The timescales of the relaxation processes will inform that the multiphase mixtures involved in the physics of detonation waves behaves essentially with a single velocity and pressure [22].

When the mesh spacing and the time step tend to zero, some averages simplify:

$$\bar{f} \to \langle f\rangle, \quad \hat{f} \to \langle f\rangle, \quad \langle\langle f\rangle\rangle \to \langle f\rangle. \tag{4.1}$$

The demonstration will be done for phase 1 only. Subscript 1 will be sometimes omitted. Eq. (3.23) is recalled:

$$\begin{aligned}&\frac{(\alpha\langle\langle W\rangle\rangle)^{n+1}_{1,ij}-(\alpha\langle\langle W\rangle\rangle)^{n}_{1,ij}}{\Delta t}+\frac{(\overline{XF})_{1,i+1/2}-(\overline{XF})_{1,i-1/2}}{\Delta x}+\frac{(\widehat{XG})_{1,j+1/2}-(\widehat{XG})_{1,j-1/2}}{\Delta y}\\ &\quad=\frac{\overline{F^{\mathrm{lag}}[X_1]}_{i+1/2}+\overline{F^{\mathrm{lag}}[X_1]}_{i-1/2}}{\Delta x}+\frac{\widehat{G^{\mathrm{lag}}[X_1]}_{j+1/2}+\widehat{G^{\mathrm{lag}}[X_1]}_{j-1/2}}{\Delta y}+na\left(\overline{F^{\mathrm{lag}}}(2,1)-\overline{F^{\mathrm{lag}}}(1,2)\right)_{ij}\\ &\qquad+na\left(\widehat{G^{\mathrm{lag}}}(2,1)-\widehat{G^{\mathrm{lag}}}(1,2)\right)_{ij}.\end{aligned} \tag{3.23}$$

It is decomposed into seven terms:

$$T_1+T_2+T_3=T_4+T_5+T_6+T_7. \tag{4.2}$$

4.1. Continuous limit of the temporal term

$$T_1=\frac{(\alpha\langle\langle W\rangle\rangle)^{n+1}_{1,ij}-(\alpha\langle\langle W\rangle\rangle)^{n}_{1,ij}}{\Delta t}\underset{\Delta t\to 0}{\to}\frac{\partial\alpha\langle W\rangle}{\partial t}=\frac{\partial\alpha W}{\partial t}. \tag{4.3}$$

4.2. Continuous limit of the horizontal convective flux

The horizontal convective flux reads:

$$T_2 = \frac{(\overline{XF})_{1,i+1/2} - (\overline{XF})_{1,i-1/2}}{\Delta x}. \tag{4.4}$$

According to (4.1), we get:

$$T_2 = \frac{(\overline{XF})_{1,i+1/2} - (\overline{XF})_{1,i-1/2}}{\Delta x} \underset{\Delta x \to 0}{\to} \frac{\partial \alpha \langle F \rangle}{\partial x} = \frac{\partial \alpha F}{\partial x}. \tag{4.5}$$

4.3. Continuous limit of the horizontal Lagrangian flux

In the x-direction, Lagrangian terms decompose into two terms T_4 and T_6. Each term is examined separately. The continuous limit of T_4 becomes horizontal non-conservative products. The continuous limit of T_6 is the horizontal relaxation term.

$$T_4 = \frac{\overline{F^{\mathrm{lag}}[X_1]}_{i+1/2} + \overline{F^{\mathrm{lag}}[X_1]}_{i-1/2}}{\Delta x}. \tag{4.6}$$

The following notations are introduced:

$$x^+ = \max(x,0) = \frac{x+|x|}{2}, \quad x^- = \min(x,0) = \frac{x-|x|}{2} \quad \text{and} \quad \delta\alpha_{1,i+1/2} = \alpha_{1,i+1} - \alpha_{1,i},$$

$$\frac{\mathrm{d}(x^+)}{\mathrm{d}x} = H(x) \quad \text{and} \quad \frac{\mathrm{d}(x^-)}{\mathrm{d}x} = -H(-x) \quad \text{such as } H \text{ the Heaviside function,}$$

$$\mathrm{sgn}(x) = \begin{cases} +1 & \text{if } x \geqslant 0, \\ -1 & \text{if } x < 0. \end{cases}$$

The Lagrangian fluxes read

$$\begin{aligned} \Delta x T_4 &= \overline{F^{\mathrm{lag}}[X_1]}_{i+1/2} + \overline{F^{\mathrm{lag}}[X_1]}_{i-1/2} \\ &= \Big(\big(\mathrm{sgn}(u^*)^+ \delta\alpha^- F^{\mathrm{lag},*}(1,2)\big)_{i-1/2} + \big(\mathrm{sgn}(u^*)^+ \delta\alpha^+ F^{\mathrm{lag},*}(2,1)\big)_{i-1/2} - \big(\mathrm{sgn}(u^*)^- \delta\alpha^- F^{\mathrm{lag},*}(1,2)\big)_{i+1/2} \\ &\quad - \big(\mathrm{sgn}(u^*)^- \delta\alpha^+ F^{\mathrm{lag},*}(2,1)\big)_{i+1/2} \Big). \end{aligned}$$

To proceed in these calculations, the various terms are developed with the help of the acoustic Riemann solver of Godunov for the Euler equations (see [39]). Consider a left state 1 and a right state 2. The pressure and velocity solution of the Riemann problem, under acoustic approximation, are given by:

$$p(1,2) = \frac{Z_2 p_1 + Z_1 p_2}{Z_1 + Z_2} + \frac{Z_1 Z_2}{Z_1 + Z_2}(u_1 - u_2) \quad \text{and} \quad u(1,2) = \frac{Z_1 u_1 + Z_2 u_2}{Z_1 + Z_2} + \frac{p_1 - p_2}{Z_1 + Z_2}. \tag{4.7a}$$

For a left state 2 and a right state 1, symmetric expressions are obtained:

$$p(2,1) = \frac{Z_2 p_1 + Z_1 p_2}{Z_1 + Z_2} + \frac{Z_1 Z_2}{Z_1 + Z_2}(u_2 - u_1) \quad \text{and} \quad u(2,1) = \frac{Z_1 u_1 + Z_2 u_2}{Z_1 + Z_2} + \frac{p_2 - p_1}{Z_1 + Z_2}, \tag{4.7b}$$

c_k and $Z_k = (\rho c)_k$ are, respectively, the sound speed and the acoustic impedance of phase k.

Such solver is valid for the present analysis because we are precisely looking for the continuous limit of the discrete equations. For such limit, it is implicitly assumed that the flow functions are smooth. Thus the acoustic solver is a correct approximation of the exact Riemann solver. At the boundary cell $i+1/2$, we have

$$u^*_{i+1/2}(1,2) = \frac{Z_1 u_{1,i} + Z_2 u_{2,i+1}}{Z_1 + Z_2} + \frac{p_{1,i} - p_{2,i+1}}{Z_1 + Z_2}.$$

Applying conventional Taylor expansions, we get

$$u_{2,i+1} \approx u_{2,i} + \Delta x \frac{\partial u_2}{\partial x} \quad \text{and} \quad p_{2,i+1} \approx p_{2,i} + \Delta x \frac{\partial p_2}{\partial x},$$

$$u^*_{i+1/2}(1,2) \approx \frac{Z_1 u_{1,i} + Z_2 u_{2,i}}{Z_1 + Z_2} + \frac{p_{1,i} - p_{2,i}}{Z_1 + Z_2} + \frac{\Delta x}{Z_1 + Z_2}\left(Z_2 \frac{\partial u_2}{\partial x} - \frac{\partial p_2}{\partial x}\right),$$

$$u^*_{i+1/2}(1,2) \approx \frac{Z_1 u_{1,i} + Z_2 u_{2,i}}{Z_1 + Z_2} + \frac{p_{1,i} - p_{2,i}}{Z_1 + Z_2} = u^*(1,2) \quad \text{at first order.}$$

In the limit $\Delta x \to 0$, $u^*_{i+1/2}(1,2) \approx u^*_{i-1/2}(1,2) \approx u^*(1,2)$ and also $u^*_{i+1/2}(2,1) \approx u^*_{i-1/2}(2,1) \approx u^*(2,1)$. The same expansion is made on the pressure. Thus the following approximations hold for the Lagrangian flux $F^{\mathrm{lag},*}_{i+1/2}(1,2) \approx F^{\mathrm{lag},*}_{i-1/2}(1,2) \approx F^{\mathrm{lag},*}(1,2)$ and $F^{\mathrm{lag},*}_{i+1/2}(2,1) \approx F^{\mathrm{lag},*}_{i-1/2}(2,1) \approx F^{\mathrm{lag},*}(2,1)$. So:

$$\begin{aligned} P\Delta x T_4 &= \overline{F^{\mathrm{lag},*}[X_1]}_{i+1/2} + \overline{F^{\mathrm{lag},*}[X_1]}_{i-1/2} \\ &= \Big(\Big(\mathrm{sgn}(u^*)^+ \delta\alpha^-_{i-1/2} - \mathrm{sgn}(u^*)^- \delta\alpha^-_{i+1/2}\Big) F^{\mathrm{lag},*}(1,2) \\ &\quad + \Big(\mathrm{sgn}(u^*)^+ \delta\alpha^+_{i-1/2} - \mathrm{sgn}(u^*)^- \delta\alpha^+_{i+1/2}\Big) F^{\mathrm{lag},*}(2,1)\Big). \end{aligned}$$

After expanding $\delta\alpha$, we get

$$\begin{aligned} \Delta x T_4 &= \overline{F^{\mathrm{lag}}[X_1]}_{i+1/2} + \overline{F^{\mathrm{lag}}[X_1]}_{i-1/2} \\ &= \left(\mathrm{sgn}(u^*)^+ \left(\delta\alpha^-_i + \frac{\Delta x}{2} H(-\delta\alpha^-_i) \frac{\partial(\delta\alpha)^-_i}{\partial x}\right) - \mathrm{sgn}(u^*)^- \left(\delta\alpha^-_i - \frac{\Delta x}{2} H(\delta\alpha^-_i) \frac{\partial(\delta\alpha)^-_i}{\partial x}\right)\right) F^{\mathrm{lag},*}(1,2) \\ &\quad + \left(\mathrm{sgn}(u^*)^+ \left(\delta\alpha^+_i - \frac{\Delta x}{2} H(-\delta\alpha^+_i) \frac{\partial(\delta\alpha)^+_i}{\partial x}\right) - \mathrm{sgn}(u^*)^- \left(\delta\alpha^-_i - \frac{\Delta x}{2} H(\delta\alpha^+_i) \frac{\partial(\delta\alpha)^+_i}{\partial x}\right)\right) F^{\mathrm{lag},*}(2,1). \end{aligned}$$

Consequently, we get,

$$\begin{aligned} \Delta x T_4 = \overline{F^{\mathrm{lag},*}[X_1]}_{i+1/2} + \overline{F^{\mathrm{lag},*}[X_1]}_{i-1/2} &= (\mathrm{sgn}(u)^+ - \mathrm{sgn}(u)^-)\delta\alpha^-_i F^{\mathrm{lag},*}(1,2) \\ &\quad + (\mathrm{sgn}(u)^+ - \mathrm{sgn}(u)^-)\delta\alpha^+_i F^{\mathrm{lag},*}(2,1), \\ \Delta x T_4 = \overline{F^{\mathrm{lag},*}[X_1]}_{i+1/2} + \overline{F^{\mathrm{lag},*}[X_1]}_{i-1/2} &= \delta\alpha^-_i F^{\mathrm{lag},*}(1,2) + \delta\alpha^+_i F^{\mathrm{lag},*}(2,1), \\ T_4 = F^{\mathrm{lag},*}_I \frac{\delta\alpha}{\Delta x}, & \end{aligned}$$

where

$$F_I^{\text{lag}} = \begin{pmatrix} u_I \\ 0 \\ p_{IX} \\ 0 \\ p_{IX}u_I \\ 0 \end{pmatrix} \quad \text{with} \quad \begin{cases} u_I = \dfrac{Z_1u_1 + Z_2u_2}{Z_1 + Z_2} + \operatorname{sgn}\left(\dfrac{\partial\alpha_1}{\partial x}\right)\dfrac{p_2 - p_1}{Z_1 + Z_2}, \\ p_{IX} = \dfrac{Z_2p_1 + Z_1p_2}{Z_1 + Z_2} + \operatorname{sgn}\left(\dfrac{\partial\alpha_1}{\partial x}\right)\dfrac{Z_1Z_2}{Z_1 + Z_2}(u_2 - u_1). \end{cases}$$

Thus when Δx tends to zero,

$$T_4 = \frac{\overline{F^{\text{lag}}[X_1]}_{i+1/2} + \overline{F^{\text{lag}}[X_1]}_{i-1/2}}{\Delta x} \underset{\Delta x \to 0}{\to} F_I^{\text{lag}} \frac{\partial\alpha}{\partial x}. \tag{4.8a}$$

Remark that we have determined a component of the average interfacial velocity u_I as well as the average of the interfacial pressure p_{IX} that exerts at the boundaries of the two-phase control volume in the x-direction. These expressions depend on the sign of the volume fraction gradient: $\operatorname{sgn}\left(\frac{\partial\alpha_1}{\partial x}\right)$. Indeed, according to its sign, either fluid 1 on the left is in contact with fluid 2 on the right or the opposite. The Riemann problem solutions (4.7a) and (4.7b) that determine the appropriate interface pressure and velocity are summarized in concise formulas depending on the sign of the volume fraction gradient.

T_6 results from the fluctuations of interface variables inside the two-phase control volume:

$$T_6 = na(F^{\text{lag}}(2,1) - F^{\text{lag}}(1,2))_{ij}$$

According to (4.7), the fluctuations of the interface velocity and pressure become

$$u(1,2) - u(2,1) = 2\frac{p_2 - p_1}{Z_1 + Z_2} \quad \text{and} \quad p(2,1) - p(1,2) = 2\frac{Z_1Z_2}{Z_1 + Z_2}(u_1 - u_2).$$

Finally,

$$T_6 = na(F^{\text{lag}}(2,1) - F^{\text{lag}}(1,2))_{ij} = \begin{pmatrix} \mu(p_1 - p_2) \\ 0 \\ \lambda(u_1 - u_2) \\ 0 \\ \lambda u_I'(u_1 - u_2) - \mu p_I'(p_1 - p_2) \\ 0 \end{pmatrix} \tag{4.8b}$$

with

$$u_I' = \frac{Z_1u_1 + Z_2u_2}{Z_1 + Z_2} \quad \text{and} \quad p_I' = \frac{Z_2p_1 + Z_1p_2}{Z_1 + Z_2}, \quad \mu = \frac{s}{2(Z_1 + Z_2)} \quad \text{and} \quad \lambda = \mu Z_1Z_2.$$

$s = 4na$ is the exchange area between the phases 1 and 2.

The same calculation are made for all the vertical fluxes.

4.4. The continuous model

From the preceding results (4.3), (4.4), (4.5), (4.8a), (4.8b) the system of PDEs for the multiphase mixture is obtained:

$$\frac{\partial\alpha_1}{\partial t} + u_I\frac{\partial\alpha_1}{\partial x} + v_I\frac{\partial\alpha_1}{\partial y} = 2\mu(p_1 - p_2), \tag{4.9a}$$

$$\frac{\partial(\alpha\rho)_1}{\partial t}+\frac{\partial(\alpha\rho u)_1}{\partial x}+\frac{\partial(\alpha\rho v)_1}{\partial y}=0, \tag{4.9b}$$

$$\frac{\partial(\alpha\rho u)_1}{\partial t}+\frac{\partial(\alpha\rho u^2+\alpha p)_1}{\partial x}+\frac{\partial(\alpha\rho uv)_1}{\partial y}=p_{IX}\frac{\partial\alpha_1}{\partial x}+\lambda(u_2-u_1), \tag{4.9c}$$

$$\frac{\partial(\alpha\rho v)_1}{\partial t}+\frac{\partial(\alpha\rho uv)_1}{\partial x}+\frac{\partial(\alpha\rho v^2+\alpha p)_1}{\partial y}=p_{IY}\frac{\partial\alpha_1}{\partial y}+\lambda(v_2-v_1), \tag{4.9d}$$

$$\begin{aligned}&\frac{\partial(\alpha\rho E)_1}{\partial t}+\frac{\partial(\alpha(\rho E+p)u)_1}{\partial x}+\frac{\partial(\alpha(\rho E+p)v)_1}{\partial y}\\&\quad=p_{IX}u_I\frac{\partial\alpha_1}{\partial x}+p_{IY}v_I\frac{\partial\alpha_1}{\partial y}+\lambda[u_I'(u_2-u_1)+v_I'(v_2-v_1)]-2\mu p_I'(p_1-p_2),\end{aligned} \tag{4.9e}$$

$$\frac{\partial(\alpha\rho Y_m)_1}{\partial t}+\frac{\partial(\alpha\rho uY_m)_1}{\partial x}+\frac{\partial(\alpha\rho vY_m)_1}{\partial y}=0. \tag{4.9f}$$

The volume fraction obeys a saturation constraint $\alpha_1+\alpha_2=1$.

The interfacial velocity has the following components:

$$u_I=u_I'+\operatorname{sgn}\left(\frac{\partial\alpha_1}{\partial x}\right)\frac{p_2-p_1}{Z_1+Z_2}\quad\text{with } u_I'=\frac{Z_1u_1+Z_2u_2}{Z_1+Z_2}, \tag{4.10}$$

$$v_I=v_I'+\operatorname{sgn}\left(\frac{\partial\alpha_1}{\partial y}\right)\frac{p_2-p_1}{Z_1+Z_2}\quad\text{with } v_I'=\frac{Z_1v_1+Z_2v_2}{Z_1+Z_2}.$$

The interfacial pressures expresses:

$$p_{IX}=p_I'+\operatorname{sgn}\left(\frac{\partial\alpha_1}{\partial x}\right)\frac{Z_1Z_2}{Z_1+Z_2}(u_2-u_1)\quad\text{and}\quad p_{IY}=p_I'+\operatorname{sgn}\left(\frac{\partial\alpha_1}{\partial y}\right)\frac{Z_1Z_2}{Z_1+Z_2}(v_2-v_1) \tag{4.11}$$

with

$$p_I'=\frac{Z_2p_1+Z_1p_2}{Z_1+Z_2}.$$

The continuous limit exhibits relaxation processes: a drag force (velocity relaxation) and a pressure relaxation.

The pressure relaxation coefficient is $\mu=\dfrac{s}{2(Z_1+Z_2)}$. (4.12)

The velocity relaxation coefficient is $\lambda=\mu Z_1Z_2$. (4.13)

The exchange area between the phases is $s=4na$. (4.14)

The multiphase equations have been found with the help of the acoustic solver. The difference between the acoustic solver and another Riemann solver is only second order. Thus the use of another Riemann solver will not change the continuous limit of the discrete equations. For these calculations, the acoustic solver was found to be the more convenient.

These results show that the average interfacial pressures and velocity that exert at the boundary of the two-phase control volume depend on the volume fraction gradient and velocity or pressure difference. These interfacial pressure and velocity are different of those applying inside the two-phase control volume. Moreover, it appears that the velocity and pressure relaxation coefficients are coupled.

4.5. Mathematical analysis of the continuous model

In one dimension, the model reads with primitive variables $V_k = (\alpha, \rho, u, v, p, Y_m)_k$,

$$\frac{\partial V_k}{\partial t} + A_k \frac{\partial V_k}{\partial x} = S_k. \tag{4.15}$$

The Jacobian matrix reads

$$A_k = \begin{pmatrix} u_I & 0 & 0 & 0 & 0 & 0 \\ \frac{\rho_k}{\alpha_k}(u_k - u_I) & u_k & \rho_k & 0 & 0 & 0 \\ \frac{p_k - p_{IX}}{\alpha_k \rho_k} & 0 & u_k & 0 & \frac{1}{\rho_k} & 0 \\ 0 & 0 & 0 & u_k & 0 & 0 \\ \frac{\rho_k c_{IX}^2}{\alpha_k}(u_k - u_I) & 0 & \rho_k c_k^2 & 0 & u_k & 0 \\ 0 & 0 & 0 & 0 & 0 & u_k \end{pmatrix} \tag{4.16}$$

with

$$c_{IX}^2 = \frac{\dfrac{p_{IX}}{\rho^2} - \dfrac{\partial e}{\partial \rho}\Big|_P}{\dfrac{\partial e}{\partial p}\Big|_\rho}$$

an interface sound speed, and the source term

$$S_k = \left(2\mu\Delta p, \frac{2\rho_k}{\alpha_k}\mu\Delta p, \frac{\lambda}{(\alpha\rho)_k}\Delta u, \frac{\lambda}{(\alpha\rho)_k}\Delta v, \frac{\lambda}{\alpha_k \frac{\partial e_k}{\partial p_k}\Big|_{\rho_k}}[(u_I - u_k)\Delta u + (v_I - v_k)\Delta v] - \frac{2\rho_k (c'_{kI})^2}{\alpha_k}\mu\Delta p, 0 \right) \tag{4.17}$$

$\Delta u = u_2 - u_1$ and $\Delta v = v_2 - v_1$ represent the velocity differences. $\Delta p = p_1 - p_2$ is the pressure difference.

The eigenvalues of the propagation matrix A_k are always real. They are: u_I interface velocity, $u_k + c_k$, $u_k - c_k$ and u_k which are the acoustic wave speeds and the speed of the contact discontinuity into the phase k.

The system of PDE is always hyperbolic. The model is also conservative regarding the mixture. All closure relations for $p_I, \vec{u}_I, \lambda$ and μ are symmetrical with respect to the phases.

4.6. Dissipative inequality

With no mass transfer, interactions between phases are given by the solution of Riemann problems. The Lagrangian fluxes at the microscopic scale give non-conservative products and relaxation terms at the macroscopic scale. We must check that these relations are compatible with the entropy inequality:

$$(\alpha\rho)_1 T_1 \frac{\mathrm{d}\eta_1}{\mathrm{d}t} + (\alpha\rho)_2 T_2 \frac{\mathrm{d}\eta_2}{\mathrm{d}t} \geqslant 0, \tag{4.19}$$

η_k represents the entropy of phase k. Following Gibbs identity we have:

$$(\alpha\rho)_k T_k \frac{\mathrm{d}\eta_k}{\mathrm{d}t} = (\alpha\rho)_k \left(\frac{\mathrm{d}e_k}{\mathrm{d}t} + p_k \frac{\mathrm{d}(1/\rho)_k}{\mathrm{d}t} \right).$$

Consider phase 1. After some algebraic manipulations, we get the internal energy equation for phase 1 ($\frac{\mathrm{d}}{\mathrm{d}t} = \frac{\partial}{\partial t} + u_k \frac{\partial}{\partial x} + v_k \frac{\partial}{\partial y}$ is the material derivative).

$$(\alpha\rho)_1 \frac{\mathrm{d}e_1}{\mathrm{d}t} + (\alpha p)_1 \left(\frac{\partial u_1}{\partial x} + \frac{\partial v_1}{\partial y} \right) = (p_{IX} - p_1)(u_I - u_1) \frac{\partial \alpha_1}{\partial x} + (p_{IY} - p_1)(v_I - v_1) \frac{\partial \alpha_1}{\partial y} + \lambda[(u_I' - u_1) \times (u_2 - u_1) + (v_I' - v_1)(v_2 - v_1)] - 2\mu p_I'(p_1 - p_2), \tag{4.20}$$

that is

$$(\alpha\rho)_1 T_1 \frac{\mathrm{d}\eta_1}{\mathrm{d}t} = (p_{IX} - p_1)(u_I - u_1) \frac{\partial \alpha_1}{\partial x} + (p_{IY} - p_1)(v_I - v_1) \frac{\partial \alpha_1}{\partial y} + \lambda[(u_I' - u_1)(u_2 - u_1) + (v_I' - v_1)(v_2 - v_1)] - 2\mu(p_I' - p_1)(p_1 - p_2). \tag{4.21}$$

We now examine the sign of the four terms on the right-hand side of this equation.

It appears that:

$$\lambda[(u_I' - u_1)(u_2 - u_1) + (v_I' - v_1)(v_2 - v_1)] = \lambda \frac{Z_2}{Z_1 + Z_2} \left[(u_2 - u_1)^2 + (v_2 - v_1)^2 \right] \geqslant 0, \tag{4.22}$$

$$2\mu(p_I' - p_1)(p_2 - p_1) = 2\mu \frac{Z_1}{Z_1 + Z_2} (p_2 - p_1)^2 \geqslant 0, \tag{4.23}$$

$$(p_{IX} - p_1)(u_I - u_1) \frac{\partial \alpha_1}{\partial x} = \frac{Z_1}{(Z_1 + Z_2)^2} \left\{ (Z_2(u_2 - u_1) + \mathrm{sgn}\left(\frac{\partial \alpha}{\partial x}\right)(p_2 - p_1)) \left(Z_2 \mathrm{sgn}\left(\frac{\partial \alpha}{\partial x}\right)(u_2 - u_1)(p_2 - p_1) \right) \right\} \frac{\partial \alpha_1}{\partial x},$$

$$(p_{IX} - p_1)(u_I - u_1) \frac{\partial \alpha_1}{\partial x} = \frac{Z_1}{(Z_1 + Z_2)^2} \left(Z_2(u_2 - u_1) + \mathrm{sgn}\left(\frac{\partial \alpha_1}{\partial x}\right)(p_2 - p_1) \right)^2 \mathrm{sgn}\left(\frac{\partial \alpha_1}{\partial x}\right) \frac{\partial \alpha_1}{\partial x} \geqslant 0, \tag{4.24a}$$

$$(p_{IY} - p_1)(v_I - v_1) \frac{\partial \alpha_1}{\partial y} = \frac{Z_1}{(Z_1 + Z_2)^2} \left(Z_2(v_2 - v_1) + \mathrm{sgn}\left(\frac{\partial \alpha_1}{\partial y}\right)(p_2 - p_1) \right)^2 \mathrm{sgn}\left(\frac{\partial \alpha_1}{\partial y}\right) \frac{\partial \alpha_1}{\partial y} \geqslant 0. \tag{4.24b}$$

Consequently, the model predicts a non-decreasing entropy for phase 1:

$$(\alpha\rho)_1 T_1 \frac{\mathrm{d}\eta_1}{\mathrm{d}t} \geqslant 0. \tag{4.25}$$

The same inequality is obtained for phase 2. As the two entropies always increase or remain constant, the entropy for the mixture defined in (4.19) also increases or remain constant. The second law of thermodynamics (4.19) is fulfilled.

4.7. Physical interpretation

The model can be written in the following way:

$$\frac{\partial(\alpha W)_k}{\partial t}+\frac{\partial(\alpha F)_k}{\partial x}+\frac{\partial(\alpha G)_k}{\partial y}=F_I^{\text{lag}}\frac{\partial \alpha_k}{\partial x}+G_I^{\text{lag}}\frac{\partial \alpha_k}{\partial y}+\text{Relax}(W) \tag{4.26}$$

such as $F_I^{\text{lag}}=(-u_I,0,p_{IX},0,p_{IX}u_I,0)$, $G_I^{\text{lag}}=(-v_I,0,0,p_{IY},p_{IY}v_I,0)$.

Let us define the operators,

$$\text{Transport}(\alpha W)=\frac{\partial(\alpha F)_k}{\partial x}-F_I^{\text{lag}}\frac{\partial \alpha_k}{\partial x}+\frac{\partial(\alpha G)_k}{\partial y}-G_I^{\text{lag}}\frac{\partial \alpha_k}{\partial y},$$

$$\text{Relax}(W)=(2\mu\Delta p,0,\lambda\Delta u,\lambda\Delta v,\lambda[u_I\Delta u+v_I\Delta v]-2p_I'\mu\Delta p,0).$$

Then we get

$$\frac{\partial(\alpha W)_k}{\partial t}+\text{Transport}(\alpha W)=\text{Relax}(W). \tag{4.27}$$

These two operators represent the crossing of the two-phase control volume by waves. Transport(αW) is a hyperbolic operator. It guarantees that the transient solution will feature waves. Typically the passage of a wave over a quiescent bed initially at thermodynamic equilibrium will cause the two phases to be brought to different states of velocity and pressure behind the wave. Processes of velocity and pressure relaxation Relax(W) will attempt to erase these differences and edge the phases towards equilibrium. Fig. 7 represents the chronology of these events. The waves will be followed by relaxation zones whose length scales depend in our model on the grain size and on the phases compressibility.

Fluctuations of the interface quantities inside the control volume give birth to relaxation processes. Fluctuations of interface velocity produce pressure relaxation. Fluctuation of interface pressure produce velocity relaxation.

$$\langle \delta p_i \nabla X_1\rangle \overset{\text{DEM}}{=} na\begin{pmatrix}\overline{p^*(2,1)}-\overline{p^*(1,2)}\\ \widehat{p^*(2,1)}-\widehat{p^*(1,2)}\end{pmatrix}\overset{\text{Continous Limit}}{\rightarrow}\lambda(\vec{u}_1-\vec{u}_2), \tag{4.28}$$

$$\langle \delta u_i \nabla X_1\rangle \overset{\text{DEM}}{=} na(\overline{u^*(2,1)}-\overline{u^*(1,2)})+na(\widehat{v^*(2,1)}-\widehat{v^*(1,2)})\overset{\text{Continuous Limit}}{\rightarrow}-2\mu(p_1-p_2). \tag{4.29}$$

A difference of pressure between the phases causes the volume fraction to vary until the two pressures be equal. This pressure difference represents the forces that act on the surface of the grains. This force works at

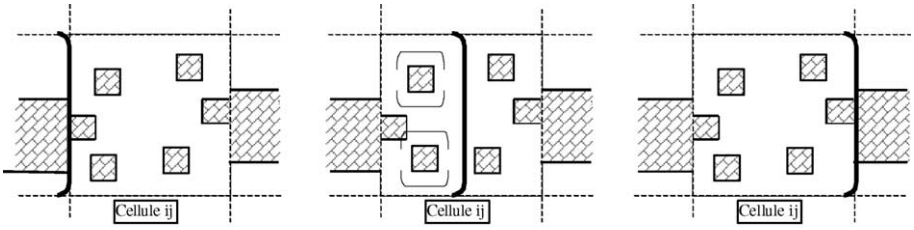

1) The wave comes into the volume 2) The wave crosses the volume 3) The wave exits the volume

Fig. 7. Chronology of the crossing of the two-phase media by a wave.

the power $2p'_I\mu(p_1 - p_2)$ at the pressure p'_I, which is the average pressure within the two-phase control volume. There is a second relaxation process represented by a drag force $\lambda(\vec{u}_2 - \vec{u}_1)$. It tends to erase the difference of velocities between phases. Its power is $\vec{u}'_I\lambda(\vec{u}_2 - \vec{u}_1)$. $\vec{u}'_I$ is the average of interface velocities within the control volume. The power of these two forces comes from

$$\langle \delta(p_i u_i)\nabla X_1\rangle \overset{\text{DEM}}{=} na\Big(\overline{(pu)^*(2,1)} - \overline{(pu)^*(1,2)}\Big) + na\Big(\widehat{(pv)^*(2,1)} - \widehat{(pv)^*(1,2)}\Big)$$

$$\overset{\text{Continuous Limit}}{\rightarrow} \lambda\big[u'_I(u_2 - u_1) + v'_I(v_2 - v_1)\big] - 2\mu p'_I(p_1 - p_2). \tag{4.30}$$

These two relaxation processes come from the presence of interfaces at the microscopic level, which tend to impose in average – at the macroscopic level – their local conditions: equality of pressure and velocity through microscopic interfaces.

Remark. In the particular case of a mixture of solid particles (phase 1) and gas (phase 2), the following hypothesis can be made $Z_1 \gg Z_2$ (the solid acoustic impedance is much greater than the gas one). This is true in atmospheric conditions. After some simplifications, conventional modelling of interfacial velocity and pressure are recovered. In a two-phase volume, the average interfacial velocity u'_I identifies with the solid velocity:

$$u'_I \approx u_1 \quad \text{and} \quad v'_I \approx v_1 \tag{4.31}$$

and the average interfacial pressure p'_I identifies with the gas pressure:

$$p'_I \approx p_2. \tag{4.32}$$

We can notice that these approximations are no longer valid in the field of detonation waves where the acoustic impedances of the different materials are of the same order.

4.8. Timescales for the relaxation processes

In the particular case of solid particles (phase 1) into a gas phase (phase 2) under atmospheric conditions, the following assumption can be made $Z_1 \gg Z_2$. After these simplifications, the signification of the relaxation coefficients is examined.

The relaxation coefficient becomes:

$$\mu \approx \frac{2\alpha_1}{Z_1 a}, \tag{4.33}$$

$$\lambda \approx \frac{2\alpha_1}{a} Z_2. \tag{4.34}$$

These coefficients can be understood with the following analysis.

Consider a solid particle at a pressure p_1 into a gas at pressure p_2. The two pressures being different, acoustic waves propagate into the solid and the gas due to a spherical shock tube. Waves propagate to the center of the solid sphere then reflect to the solid–gas interface (see Figs. 8 and 9).

The characteristic time for the two pressures to equilibrate is of the order of $\tau_{\text{relaxP}} = 2a/c_1$, a is here the radius of the particle and c_1 is the sound speed of the solid phase. We have

$$\frac{\partial a}{\partial t} = u_{p,i}, \quad u_{p,i} \text{ the interfacial velocity of the particle}$$

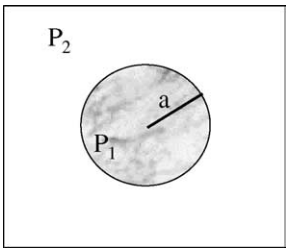

Fig. 8. Spherical solid particle into a gas.

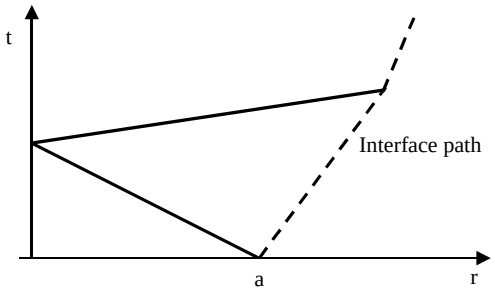

Fig. 9. Wave diagram (r,t).

The Newton's law gives $\rho_1 \frac{\partial u_p}{\partial t} = \nabla p$, where u_p is the radial velocity inside the particle. Then $\rho_1 \frac{u_{p,i}}{\tau_{\text{relaxP}}} \propto \frac{\Delta p}{a}$, where Δp is the difference between the solid pressure and the gas pressure.

$$\frac{\partial a}{\partial t} \propto \frac{\Delta p}{\rho_1} \frac{\tau_{\text{relaxP}}}{a} \quad \text{with } \tau_{\text{relaxP}} = 2a/c_1$$

then

$$\frac{\partial a}{\partial t} \propto \frac{\Delta p}{\rho_1 c_1}.$$

As $\alpha_1 = na^2$, n is the number of particles per volume unit. The following assessment holds

$$\frac{\partial \alpha}{\partial t} \propto \frac{2\alpha_1}{a} \frac{\Delta P}{(\rho c)_1},$$

which defines the following pressure relaxation coefficient $\mu = \frac{2\alpha_1}{Z_1 a}$. In this case, the discrete equations method provides the same estimate for this coefficient (4.33).

There is a correlation between the pressure relaxation and the velocity relaxation. The latter is modelled by a pressure drag $\lambda(u_2 - u_1)$ that comes from the fluctuations of the pressures along the surface of the particle. As the phases velocities are different, the upstream pressure is different from the downstream pressure.

Estimation of the velocity relaxation time can be done as follows:

$$\frac{\partial(\alpha\rho u)_1}{\partial t} = \lambda(u_2 - u_1),$$

$$\frac{\partial u_1}{\partial t} = \frac{\lambda}{(\alpha\rho)_1}(u_2 - u_1), \quad \text{i.e.,} \quad \frac{\partial u_1}{\partial t} = \frac{(u_2 - u_1)}{\tau_{\text{relaxU}}} \text{ and implies } \tau_{\text{relaxU}} = \frac{(\alpha\rho)_1}{\lambda}.$$

By using (4.34), we have the following estimate: $\tau_{\text{relaxU}} = \tau_{\text{relaxP}} \frac{Z_1}{Z_2}$.

Thus, in the limit $Z_1 \gg Z_2$, the timescale for velocity relaxation is much higher that the timescale for pressure relaxation. In the case of solid particles of $a = 100$ μm, density $\rho_1 \approx 5 \times 10^3$ kg/m^3 and sound speed of 5×10^3 m/s in a gas under atmospheric conditions, we have

$$\tau_{\text{relaxP}} \propto 10^{-8} \text{ s} \quad \text{and} \quad \tau_{\text{relaxU}} \propto 10^8 \tau_{\text{relaxP}} = 1 \text{ s}.$$

Thus the relaxation velocity under atmospheric conditions is very high compared to the pressure relaxation timescale.

Consider now detonation conditions. The gas phase comes from the solid phase decomposition and is at high temperature and density. Thus the assumption $Z_1 \gg Z_2$ no longer holds. In this case, we suppose that the characteristic time for pressure relaxation is $\tau_{\text{relaxP}} = 2a/c_1$. During the detonation propagation, Z_1 and Z_2 are of the same order of magnitude. The velocity relaxation time scale $\tau_{\text{relaxU}} = \frac{(\alpha\rho)_1}{\lambda}$ becomes

$$\tau_{\text{relaxU}} = \frac{\rho_1 a(Z_1 + Z_2)}{2Z_1 Z_2}.$$

Thus,

$$\tau_{\text{relaxU}} \propto \tau_{\text{relaxP}}.$$

The velocity relaxation timescale is of the same order as the pressure relaxation timescale. The pressure relaxation timescale τ_{relaxP} under detonation conditions remains of the same order as under atmospheric conditions ($\tau_{\text{relaxP}} \propto 10^{-8}$ s). This timescale is much smaller than the characteristic timescale of the events under study. Indeed, this model is developed for an accurate computation of the detonation propagation at the macroscopic scale.

For this type of applications, the analysis of the timescales of pressure and velocity relaxation compared to macroscopic timescale justifies the use of numerical procedures with infinite rate of velocity and pressure relaxation. Such procedure will be described in Section 5.

4.9. Model limitations

As mentioned in Section 1 and just before, this model has been derived for the propagation regime of detonation waves in condensed heterogeneous energetic materials. The propagation of this detonation wave is always coupled to the interactions with surrounding materials. Thus, it is mandatory that interface problems be solved in conjunction with the detonation dynamics. The present method fulfills these two goals.

Moreover, the multiphase method has another benefit. The model does not need mixture equation of state, that are always based on limited validity assumptions. Only the pure phase equations of state are used in conjunction with relaxation processes.

However, this model cannot be considered valid for the ignition and growth events that occur in condensed energetic materials. During ignition for example, part of the shock energy is focused into the material heterogeneities (pores for example) and the ignition results from microscale phenomena: viscoplastic pore collapse, shear banding, etc. Such phenomena involve solid–solid phase transitions accompanied by volumes changes, grain cracking, melting, low Reynolds number flows, etc. Such microscale effects correspond to the so-called hot spots formation. It is clear that such events include extra physics compared to the Euler equations. They are not considered in the present model and are out of the scope of this paper.

It is worth to mention that in the context of such sophisticated modelling, micro-mechanical models have to be coupled with a macro-scale model for waves propagation. Such issue has been addressed in Massoni et al. (1999). The macroscopic multiphase model was composed of the mixture Euler equations. As mentioned in the same reference, such model could be improved by replacing the macroscopic system by a model closed to the present one. A first attempt of this type of coupling was done in Gavrilyuk and Saurel [18], in the simplified situation of inert bubbly liquids with micro-inertia. Further investigations are necessary for the building of a multiphase model with microstructure valid for ignition, growth and propagation of the detonation.

5. Numerical strategy

In detonation propagation applications, the relaxation processes timescales are very short compared to the timescales of wave propagation. For numerical stability reasons, direct resolution of this model will induce small time steps. We propose a splitting strategy to get free of this constraint. The same remark holds for the mass transfer and chemical kinetics terms that are associated with their own timescales.

A splitting strategy is adopted that insures the stability of each step. Obviously, such strategy is not free of inaccuracy, but it seems to be the only reasonable procedure in the context of the complex physics we have to deal with.

The model to solve can be summarized in the following way:

$$\frac{\partial(\alpha W)_k}{\partial t}+\frac{\partial(\alpha F)_k}{\partial x}+\frac{\partial(\alpha G)_k}{\partial y}=F_I^{\text{lag}}\frac{\partial \alpha_k}{\partial x}+G_I^{\text{lag}}\frac{\partial \alpha_k}{\partial y}+\text{Relax}(W)+\text{Mass}(\alpha W), \tag{5.1}$$

where the various vectors have already been defined except $\text{Mass}(\alpha W)$

$$\text{Mass}(\alpha W)=\left(\frac{\dot{m}_k}{\rho_{\text{IR}}},\dot{m}_k,\dot{m}_k\vec{u}_I',\dot{m}_kE_{\text{IR}},\dot{m}_{mk}\right). \tag{5.2}$$

As already suggested by Baer and Nunziato [3] and Kapila et al. [22], the variables with subscript IR are those of the solid phase ($\text{IR}=1$).

Better estimates for these variables can be obtained with the discrete equations method when each conventional Riemann problem is replaced at the various interfaces by a reactive Riemann problem [10,19]. Such approach has been developed in LeMetayer et al. [27] in the context of evaporation waves. In our context, the kinetic relation as well as the EOS being rather complex, the approach based on a reactive Riemann solver is non-trivial. So we retain the estimates given previously.

Eq. (5.1) is then approximated by a second-order dimensional splitting [37]:

$$(\alpha W)^{n+2}=L_y(\Delta t)L_x(\Delta t)L_x(\Delta t)L_y(\Delta t)(\alpha W)^n. \tag{5.3}$$

Each one-dimensional L (L_x or L_y) operator is the composition of three operators:

$$L(\Delta t)=\text{Transport}(\Delta t)(s\text{Relax})(\Delta t/2)\text{Mass}(\Delta t/2) \tag{5.4}$$

Transport represents the one-dimensional hyperbolic non-conservative solver. Relax represents the relaxation solver. Mass represents the mass transfer solver.

As explained previously, the relaxation processes can be very fast compared to those of Transport. Then an equilibrium procedure that assumes that the relaxation timescales tend to zero is applied. An example of such procedure is given in Saurel and LeMetayer [34]. A detailed review of the optimal different numerical procedures is given in Lallemand et al. [25]. In particular, the latter paper addresses general EOS, situations involving a large number of phases and in some specific situations, exact procedures are available.

The stiffness of the mass transfer appears when the characteristic timescale of the chemical decomposition is very small compared to the characteristic timescale of the transport step. The chemical solver must be accurate enough to maintain the accuracy of the coupled solution. To successfully integrate a stiff system of chemical equations, a method with a variable local time step must be employed in order to maintain accuracy. But the method must not be limited by fast timescales once they have decayed sufficiently. Additionally, the use of a stiff integrator in a reacting-flow code require the minimum start-up cost. The solver CHEMEQ2 meets all these requirements. Moreover, it has been specially designed for the integration of chemical decomposition in a process-split approach. Mott et al. [30] have recently proposed this method. It is a predictor–corrector scheme based on a Quasi-Steady-State-Approximation (QSSA). Its accuracy has been proved to be second order on the overall time step Δt. The local time step selection is automatically managed and its management is the same as proposed in [40].

The two preceding operators Relax and Mass require careful treatment as provided in the cited references. Analysis of these operators comes out of the scope of the present paper. We prefer to provide more details about the Transport step in the context of the detonation hydrocode that will be used for the applications.

The basic ideas and formulas necessary for the development of *Transport* have already been derived in Section 3. The details of its implementation and extension to second order are now summarized.

(a) *Predictor step*

(a.1) At each cell boundary, the length of contact is computed by the formulas of Tables 1 and 2 according to the local volume fraction gradient. When dealing with an arbitrary number of phases the corresponding length of contact are obtained by following the procedure given in Appendix C. The numerical procedure that follows extends easily to such general situation. For the sake of clarity we restrict the description to two phases only.

(a.2) In each cell, the primitive variables for the phase k are denoted $V_{k,i} = (\alpha, \rho, u, v, p, \{Y_m\})_{k,i}$. At each cell boundary Riemann problems are solved for each fluid pair (p, q). The convective flux along $x/t = 0$ is stored in $F^*(p,q)$ as well as each Lagrangian flux along $x/t = u^*(p,q)$ and stored in $F^{\mathrm{lag},*}(p,q)$.

(a.3) According to the sign of $u^*(p,q)$ solution of the Riemann problem, the phase function $X_k^*(p,q)$ is obtained as well as the jump $[X_k^*(p,q)]$. Note that for $k \neq p$ and $k \neq q$, $X_k^*(p,q)$ and the jump $[X_k^*(p,q)]$ are always zero. The other instances are described in Tables 1 and 2.

(a.4) All the ingredients are now available to estimate the solution at the intermediate time step $t^{n+1/2}$:

$$\frac{(\alpha W)_{1,i}^{n+1/2} - (\alpha W)_{1,i}^{n}}{\Delta t/2} + \frac{(\overline{XF})_{1,i+1/2}^{n} - (\overline{XF})_{1,i-1/2}^{n}}{\Delta x} = \frac{\overline{F^{\mathrm{lag}}[X_1]}_{i+1/2}^{n} + \overline{F^{\mathrm{lag}}[X_1]}_{i-1/2}^{n}}{\Delta x}, \tag{5.5}$$

$$\begin{aligned}\overline{XF}_{1,i+1/2}^{n} = {} & \max(0; \alpha_{1,i}^{n} - \alpha_{1,i+1}^{n}) X_{1,i+1/2}^{*}(1,2) F_{i+1/2}^{*}(1,2) + \min(\alpha_{1,i+1}^{n}; \alpha_{1,i}^{n}) X_{1,i+1/2}^{*}(1,1) F_{i+1/2}^{*}(1,1) \\ & + \max(0; \alpha_{1,i+1}^{n} - \alpha_{1,i}^{n}) X_{1,i+1/2}^{*}(2,1) F_{i+1/2}^{*}(2,1),\end{aligned} \tag{5.6a}$$

$$\begin{aligned}\overline{XF}_{1,i-1/2}^{n} = {} & \max(0; \alpha_{1,i-1}^{n} - \alpha_{1,i}^{n}) X_{1,i-1/2}^{*}(1,2) F_{i-1/2}^{*}(1,2) + \min(\alpha_{1,i}^{n}; \alpha_{1,i-1}^{n}) X_{1,i-1/2}^{*}(1,1) F_{i-1/2}^{*}(1,1) \\ & + \max(0; \alpha_{1,i}^{n} - \alpha_{1,i-1}^{n}) X_{1,i-1/2}^{*}(2,1) F_{i-1/2}^{*}(2,1),\end{aligned} \tag{5.6b}$$

$$\begin{aligned}\overline{F^{\mathrm{lag}}[X_1]}_{i+1/2}^{n} = {} & \max(0; \alpha_{1,i}^{n} - \alpha_{1,i+1}^{n}) [X_1]_{i+1/2}^{*}(1,2) F_{i+1/2}^{\mathrm{lag},*}(1,2) \\ & + \max(0; \alpha_{1,i+1}^{n} - \alpha_{1,i}^{n}) [X_1]_{i+1/2}^{*}(2,1) F_{i+1/2}^{*}(2,1),\end{aligned} \tag{5.6c}$$

$$\begin{aligned}\overline{F^{\mathrm{lag}}[X_1]}_{i-1/2}^{n} = {} & \max(0; \alpha_{1,i-1}^{n} - \alpha_{1,i}^{n}) [X_1]_{i-1/2}^{*}(1,2) F_{i-1/2}^{\mathrm{lag},*}(1,2) \\ & + \max(0; \alpha_{1,i}^{n} - \alpha_{1,i-1}^{n}) [X_1]_{i-1/2}^{*}(2,1) F_{i-1/2}^{\mathrm{lag},*}(2,1).\end{aligned} \tag{5.6d}$$

The convective and Lagrangian fluxes are computed as detailed in (a.2) with the initial states of time t^n: $F^*_{i+1/2}(p,q) = \mathscr{RP}(V^n_{p,i}, V^n_{q,i+1})$ and $F^{\mathrm{lag},*}_{i+1/2}(p,q) = \mathscr{RP}(V^n_{p,i}, V^n_{q,i+1})$. In the context of detonation waves, it is recommended to use a non-linear Riemann solver, such as the HLLC solver of Toro [39] rather than a linearized one, as the acoustic one used for the continuous limit determination.

(b) *Variables extrapolation*

(b.1) In each cell, the slope of the primitive variables $\delta V^{n+1/2}_{k,i}$ are computed with a conventional limiter procedure. Note that α_k is one of these variables. It means that the cell contains a volume fraction gradient.

(b.2) Extrapolation of the variables on the cell boundary is done in a conventional way as follows:

$$V^n_{k,i-1/2,\mathrm{R}} = V^n_{k,i} - \frac{\delta V^n_{k,i}}{2} \quad \text{and} \quad V^n_{k,i+1/2,\mathrm{L}} = V^n_{k,i} + \frac{\delta V^n_{k,i}}{2} \tag{5.7}$$

from which the conservatives variables are deduced $(\alpha W)^n_{k,i-1/2,\mathrm{R}}$ and $(\alpha W)^n_{k,i+1/2,\mathrm{L}}$.

(b.3) From these variables, Riemann problem solutions and the different convective and Lagrangian fluxes are computed as previously detailed in (a.2). The phase function at cell boundary are also determined as in (a.3).

(c) *Corrector step*

The solution is updated by:

$$\frac{(\alpha W)^{n+1}_{1,i} - (\alpha W)^n_{1,ij}}{\Delta t} + \frac{(\overline{XF})^{n+1/2}_{1,i+1/2} - (\overline{XF})^{n+1/2}_{1,i-1/2}}{\Delta x} = \frac{\overline{F^{\mathrm{lag}}[X_1]}^{n+1/2}_{i+1/2} + \overline{F^{\mathrm{lag}}[X_1]}^{n+1/2}_{i-1/2}}{\Delta x} + \frac{\overline{F^{\mathrm{lag}}[X_1]}^{n+1/2}_{i}}{\Delta x}, \tag{5.7}$$

$$\begin{aligned}\overline{XF}^{n+1/2}_{1,i+1/2} = {} & \max(0; \alpha^{n+1/2}_{1,i+1/2\mathrm{L}} - \alpha^{n+1/2}_{1,i+1/2\mathrm{R}}) X^*_{1,i+1/2}(1,2) F^*_{i+1/2}(1,2) \\ & + \min(\alpha^{n+1/2}_{1,i+1/2\mathrm{R}}; \alpha^{n+1/2}_{1,i+1/2\mathrm{L}}) X^*_{1,i+1/2}(1,1) F^*_{i+1/2}(1,1) \\ & + \max(0; \alpha^{n+1/2}_{1,i+1/2\mathrm{R}} - \alpha^{n+1/2}_{1,i+1/2\mathrm{L}}) X^*_{1,i+1/2}(2,1) F^*_{i+1/2}(2,1),\end{aligned} \tag{5.8a}$$

$$\begin{aligned}\overline{XF}^{n+1/2}_{1,i-1/2} = {} & \max(0; \alpha^{n+1/2}_{1,i-1/2\mathrm{L}} - \alpha^{n+1/2}_{1,i-1/2\mathrm{R}}) X^*_{1,i-1/2}(1,2) F^*_{i-1/2}(1,2) \\ & + \min(\alpha^{n+1/2}_{1,i-1/2\mathrm{R}}; \alpha^{n+1/2}_{1,i-1/2\mathrm{L}}) X^*_{1,i-1/2}(1,1) F^*_{i-1/2}(1,1) \\ & + \max(0; \alpha^{n+1/2}_{1,i-1/2\mathrm{R}} - \alpha^{n+1/2}_{1,i-1/2\mathrm{L}}) X^*_{1,i-1/2}(2,1) F^*_{i-1/2}(2,1),\end{aligned} \tag{5.8b}$$

$$\begin{aligned}\overline{F^{\mathrm{lag}}[X_1]}^{n+1/2}_{i+1/2} = {} & \max(0; \alpha^{n+1/2}_{1,i+1/2\mathrm{L}} - \alpha^{n+1/2}_{1,i+1/2\mathrm{R}}) [X_1]^*_{i+1/2}(1,2) F^{\mathrm{lag}*}_{i+1/2}(1,2) \\ & + \max(0; \alpha^{n+1/2}_{1,i+1/2\mathrm{R}} - \alpha^{n+1/2}_{1,i+1/2\mathrm{L}}) [X_1]^*_{i+1/2}(2,1) F^*_{i+1/2}(2,1),\end{aligned} \tag{5.8c}$$

$$\begin{aligned}\overline{F^{\mathrm{lag}}[X_1]}^{n+1/2}_{i-1/2} = {} & \max(0; \alpha^{n+1/2}_{1,i-1/2L} - \alpha^{n+1/2}_{1,i-1/2\mathrm{R}}) [X_1]^*_{i-1/2}(1,2) F^{\mathrm{lag},*}_{i-1/2}(1,2) \\ & + \max(0; \alpha^{n+1/2}_{1,i-1/2\mathrm{R}} - \alpha^{n+1/2}_{1,i-1/2\mathrm{L}}) [X_1]^*_{i-1/2}(2,1) F^{\mathrm{lag},*}_{i-1/2}(2,1),\end{aligned} \tag{5.8d}$$

$$\begin{aligned}\overline{F^{\mathrm{lag}}[X_1]}^{n+1/2}_{i} = {} & \max(0; \alpha^{n+1/2}_{1,i-1/2\mathrm{R}} - \alpha^{n+1/2}_{1,i+1/2\mathrm{L}}) [X_1]^*_{i-1/2}(1,2) F^{\mathrm{lag},*}_{i}(1,2) \\ & + \max(0; \alpha^{n+1/2}_{1,i+1/2\mathrm{L}} - \alpha^{n+1/2}_{1,i-1/2\mathrm{R}}) [X_1]^*_{i-1/2}(2,1) F^{\mathrm{lag},*}_{i-1/2}(2,1).\end{aligned} \tag{5.8e}$$

Within the corrector step, the convective and Lagrangian fluxes are computed as follows $F^*_{i+1/2}(p,q) = \mathscr{RP}(V^{n+1/2}_{p,i+1/2\mathrm{L}}, V^{n+1/2}_{q,i+1/2\mathrm{R}})$ and $F^{\mathrm{lag},*}_{i+1/2}(p,q) = \mathscr{RP}(V^{n+1/2}_{p,i+1/2\mathrm{L}}, V^{n+1/2}_{q,i+1/2\mathrm{R}})$.

The corrector step is a trivial extension of formulas (5.5) and (5.6). Due to the presence of the internal volume fraction gradient, a correction must be added $\overline{F^{\mathrm{lag}}[X_1]}_i^{n+1/2}$. The internal Lagrangian flux is computed as follows: $F_i^{\mathrm{lag},*}(p,q) = \mathscr{R}\mathscr{P}(V_{p,i-1/2\mathrm{R}}^{n+1/2}, V_{q,i+1/2\mathrm{L}}^{n+1/2})$. This term is explained in Abgrall and Saurel [2].

6. Properties of the discrete hyperbolic operator

We address the issue of numerical stability of the Transport operator, that is its CFL stability condition. Then, we show that under this constraint, the volume fraction is always bounded.

6.1. Constraint on the time step

The transport step reduces to

$$(\alpha W)_{1,i}^{n+1} = (\alpha W)_{1,i}^{n} - \frac{\Delta t}{\Delta x}\left(\sum_{q,r=1,2} S_{q_i,r_{i+1}} \left((X^*F^*)_1 - F^{\mathrm{lag},*}[X_1^*] \right)_{i+1/2}(q_i, r_{i+1}) \right.$$
$$\left. - \sum_{p,q=1,2} S_{p_{i-1},q_i} \left((X^*F^*)_1 - F^{\mathrm{lag},*}[X_1^*] \right)_{i-1/2}(p_{i-1}, q_i) \right). \tag{6.1}$$

Here q_i is the state of the fluid q in the cell i. r_{i+1} is the state of the fluid r in the cell $i+1$. p_{i-1} is the state of fluid p in cell $i-1$. We note $(X^*F^*)_1 - F^{\mathrm{lag},*}[X_1^*] = F^{\mathrm{num}}$ and $\theta = \frac{\Delta t}{\Delta x}$ the Courant number.

$$(\alpha W)_{1,i}^{n+1} = (\alpha W)_{1,i}^{n} - \theta \quad \sum_{q,r=1,2} S_{q_i,t2}$$

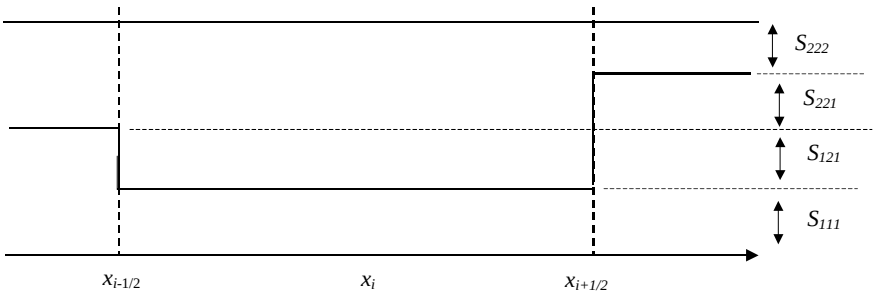

Fig. 10. Schematic representation of a possible configuration.

$F^{\text{num}}_{i+1/2}(2,2) = F^{\text{num}}_{i-1/2}(2,2) = 0$ because the indicator function X_1 is 0 inside the fluid 2.

$$\begin{aligned}(\alpha W)^{n+1}_{k,i} &= S_{111}((XW)_1 - \theta(F^{\text{num}}_{i+1/2}(1,1) - F^{\text{num}}_{i-1/2}(1,1)) + S_{121}(0 - \theta(F^{\text{num}}_{i+1/2}(2,1) - F^{\text{num}}_{i-1/2}(1,2))\\ &\quad + S_{221}(0 - \theta(F^{\text{num}}_{i+1/2}(1,2) - F^{\text{num}}_{i-1/2}(2,2)) + S_{222}(0 - \theta(F^{\text{num}}_{i+1/2}(2,2) - F^{\text{num}}_{i-1/2}(2,2)),\end{aligned} \tag{6.6}$$

$$(\alpha W)^{n+1}_{k,i} = S_{111}((XW)^{n+1}_{1,i})_{111} + S_{121}((XW)^{n+1}_{1,i})_{121} + S_{221}((XW)^{n+1}_{1,i})_{221} + S_{222}((XW)^{n+1}_{1,i})_{222}. \tag{6.7}$$

The evolution of the numerical variables $((X_k W)^{n+1}_i)_{pqr}$ is given by a numerical projection.

$((X_k W)^{n+1}_i)_{pqr}$ is a Godunov numerical scheme on a fixed grid (see Fig. 11):

$$((XW)^{n+1}_{1,i})_{pqr} = \frac{1}{x_{i+1/2} - x_{i-1/2}} \int_{x_{i-1/2}}^{x_{i+1/2}} (XW)^{n+1}_{1,i}(x, t^{n+1})\,\mathrm{d}x. \tag{6.8}$$

The formula (6.8) is valid as long as the waves coming from the boundaries $i - 1/2$ and $i + 1/2$ do not cross each other during the time step Δt. Thus,

$$\frac{\Delta t}{\Delta x} \max_k (|u| + c)_k \leqslant 1/2. \tag{6.9}$$

As $S_{111} + S_{121} + S_{221} + S_{222} = 1$, the macroscopic variables αW at time t^{n+1} are obtained by a convex average of the variables αW at time t^n. Thus under the CFL condition (6.9), we get the positivity of the partial density. We get the same CFL condition in the other configurations.

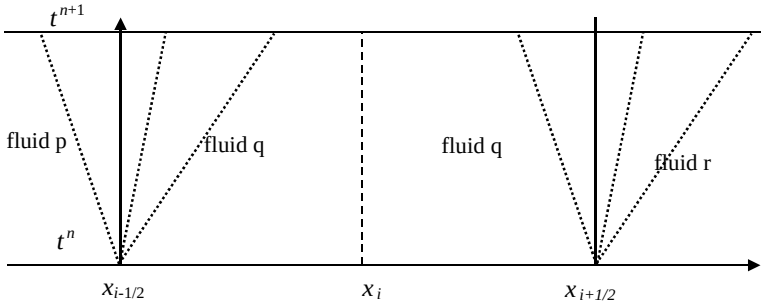

Fig. 11. Evolution of the variables $((XW)^{n+1}_{1,i})_{pqr}$ in the (x,t) diagram.

6.2. Boundedness of the volume fraction

The volume fraction must be bounded: $0 < \alpha_{k,i}^{n+1} < 1$. The numerical scheme for the volume fraction is deduced from (3.23):

$$\alpha_{1,i}^{n+1} = \alpha_{1,i}^{n} - \theta\Big\{u_{i-1/2}^{+}(1,2)(\alpha_{1,i-1}-\alpha_{1,i})^{+}(-1) + u_{i-1/2}^{+}(2,1)(\alpha_{1,i}-\alpha_{1,i-1})^{+}(+1) + u_{i+1/2}^{-}(1,2)(\alpha_{1,i}-\alpha_{1,i+1})^{+}(-1) + u_{i+1/2}^{-}(2,1)(\alpha_{1,i+1}-\alpha_{1,i})^{+}(+1)\Big\}.$$

We must investigate four cases.

The first case is $\alpha_{1,i-1} - \alpha_{1,i} \geqslant 0$ and $\alpha_{1,i} - \alpha_{1,i+1} \geqslant 0$.

In this case, the numerical scheme for the volume fraction is:

$$\alpha_{1,i}^{n+1} = \alpha_{1,i}^{n} - \theta\{-u_{i-1/2}^{+}(1,2)(\alpha_{1,i-1}-\alpha_{1,i}) - u_{i+1/2}^{-}(1,2)(\alpha_{1,i}-\alpha_{1,i+1})^{+}\}$$

that can be written in the incremental form

$$\alpha_{1,i}^{n+1} = \alpha_{1,i}^{n}(1 - \theta u_{i-1/2}^{+}(1,2) + \theta u_{i+1/2}^{-}(1,2)) + \theta u_{i-1/2}^{+}(1,2)\alpha_{1,i-1} + \theta u_{i+1/2}^{-}(1,2)\alpha_{1,i+1}.$$

Thus according to the Harten's criteria [19, p. 169], we get

$$\min(\alpha_{1,i-1}^{n}, \alpha_{1,i}^{n}, \alpha_{1,i+1}^{n}) \leqslant \alpha_{1,i}^{n+1} \leqslant \max(\alpha_{1,i-1}^{n}, \alpha_{1,i}^{n}, \alpha_{1,i+1}^{n})$$

if $0 \leqslant (1 - \theta u_{i-1/2}^{+}(1,2) + \theta u_{i+1/2}^{-}(1,2)) \leqslant 1$. This condition is fulfilled if the numerical scheme verifies the CFL condition.

The second case is $\alpha_{1,i-1} - \alpha_{1,i} \geqslant 0$ and $\alpha_{1,i} - \alpha_{1,i+1} \leqslant 0$.

In this case, the numerical scheme for the volume fraction is:

$$\alpha_{1,i}^{n+1} = \alpha_{1,i}^{n} - \theta\{-u_{i-1/2}^{+}(1,2)(\alpha_{1,i-1}-\alpha_{1,i}) + u_{i+1/2}^{-}(2,1)(\alpha_{1,i+1}-\alpha_{1,i})\}$$

that can be written in the incremental form

$$\alpha_{1,i}^{n+1} = \alpha_{1,i}^{n}(1 - \theta u_{i-1/2}^{+}(1,2) + \theta u_{i+1/2}^{-}(2,1)) + \theta u_{i-1/2}^{+}(1,2)\alpha_{1,i-1} + \theta u_{i+1/2}^{-}(2,1)\alpha_{1,i+1}.$$

Thus

$$\min(\alpha_{1,i-1}^{n}, \alpha_{1,i}^{n}, \alpha_{1,i+1}^{n}) \leqslant \alpha_{1,i}^{n+1} \leqslant \max(\alpha_{1,i-1}^{n}, \alpha_{1,i}^{n}, \alpha_{1,i+1}^{n})$$

if $0 \leqslant (1 - \theta u_{i-1/2}^{+}(1,2) + \lambda u_{i+1/2}^{-}(1,2)) \leqslant 1$. Again, this condition is fulfilled if the numerical scheme verifies the CFL condition.

The two other cases are symmetrical.

7. Validation and test cases

The numerical model for multiphase flows is validated over different problems involving interfaces, shock and detonation waves in one and two space dimensions. Each feature of the model and method is tested over a separated effects test and is compared with an exact or experimental solution.

The shock tube test case is used to validate the method for interface problems. The shock propagation into solid mixtures test is used to validate the thermodynamic properties of the model. Without knowing the equation of state of the mixture, the shock wave is correctly propagated by using only the pure materials equations of state and relaxation parameters. Then the calculation of the detonation reaction zone for an

idealized explosive is examined. It is shown that the method computes correctly this wave by comparing the numerical predictions versus the exact solution. We then consider problems where all these effects are coupled: interfaces, mixture thermodynamics and detonations. The first of these two tests illustrates the model capabilities in 1D and the second one consider a hypervelocity impact and detonation propagation in 2D.

7.1. Water–air shock tube

The solution of a 1D shock tube problem involving two different phases is presented: the high-pressure chamber contains liquid water and the low-pressure chamber is filled with air. The aim of this test is to show that the multiphase model and the numerical method are able to deal with contact/interfaces problems. When such a test is done with the Euler equations and conservative schemes, since the equation of state parameters of the two fluids are discontinuous at the interface (Table 3), conventional methods fail at the second time step. The reason is that an artificial mixture has been created at the interface, for which the computation of the pressure, sound speed is problematic. This issue has been addressed by many researchers: Karni [23,24], Abgrall [1], Shyue [36], Fedkiw et al. [14], Saurel and Abgrall [32,33], etc. With the present method, each fluid evolves in its own volume and remains separated from the others even in the artificial diffusion zones. Moreover, the non-conservative and relaxation terms are able to insure the interface conditions (equality of pressure and velocity). The initial interface that separates the liquid (at left) and the gas (at right), is set at the position $x = 0.7$ m, and the total length of the tube is equal to 1m. At the initial time, the thermodynamic conditions of the liquid are: the pressure is 10^8 Pa, the density is 1000 kg/m^3, and the temperature is 373 K. The pressure of the gas is 10^5 Pa, its density is equal to 50 kg/m^3 and the temperature is 300 K. The right and left chambers contain nearly pure fluids: the volume fraction of gas in the water chamber is 10^{-8} and vice versa in the gas chamber. This small amount of the minor phase is due to the multiphase feature of the model.

Because fluids are almost pure here and there the initial interface an exact solution is available and will be used for analysing the accuracy of the computed results.

The liquid water and the gas are governed by a modified stiffened gas equation of state: $e = e_0 + \frac{p+\gamma p_\infty}{(\gamma-1)\rho} - \frac{p_0+\gamma p_\infty}{(\gamma-1)\rho_0}$. The subscript 0 denotes a standard state. This form allows the calculation of the temperature of the different phases, given by the following formula:

$$T = \frac{1}{C_v}\left(e - e_0 + \frac{p_0 + \gamma p_\infty}{(\gamma-1)\rho_0} - \frac{p_\infty}{\rho} - \left(\frac{\rho}{\rho_0}\right)^{\gamma-1}\left(\frac{p_0+\gamma p_\infty}{(\gamma-1)\rho_0} - C_v T_0\right)\right).$$

The various parameters of the EOS are given in Table 3.

Two simulations are performed with a different grid resolution: a coarse mesh with 100 cells while a fine grid resolution uses 1000 cells. The numerical results are plotted at time 237.44 μs.

In Fig. 12, the main quantities of the flow are plotted : pressure, velocity, mixture density and temperature. A direct comparison with the analytical solution can be made. The mixture temperature is plotted. The mixture temperature is computed from the relation: $T_m = \frac{\sum_k (\alpha\rho C_v T)_k}{\sum_k (\alpha\rho C_v)_k}$. Whatever the grid resolution the numerical temperature is free of oscillation. Mesh convergence of the temperature can be obtained, as pointed by the resolution with the fine mesh. The distance between the interface and the shock being very

Table 3
Parameters of the EOS of liquid water and air for the shock tube problem

	p_∞ (Pa)	γ	C_v (J/kg/K)	e_0 (J/kg)	ρ_0 (kg/m^3)
Liquid	6×10^8	4.4	4180	617	1000
Gas	0	1.4	1000	0	50

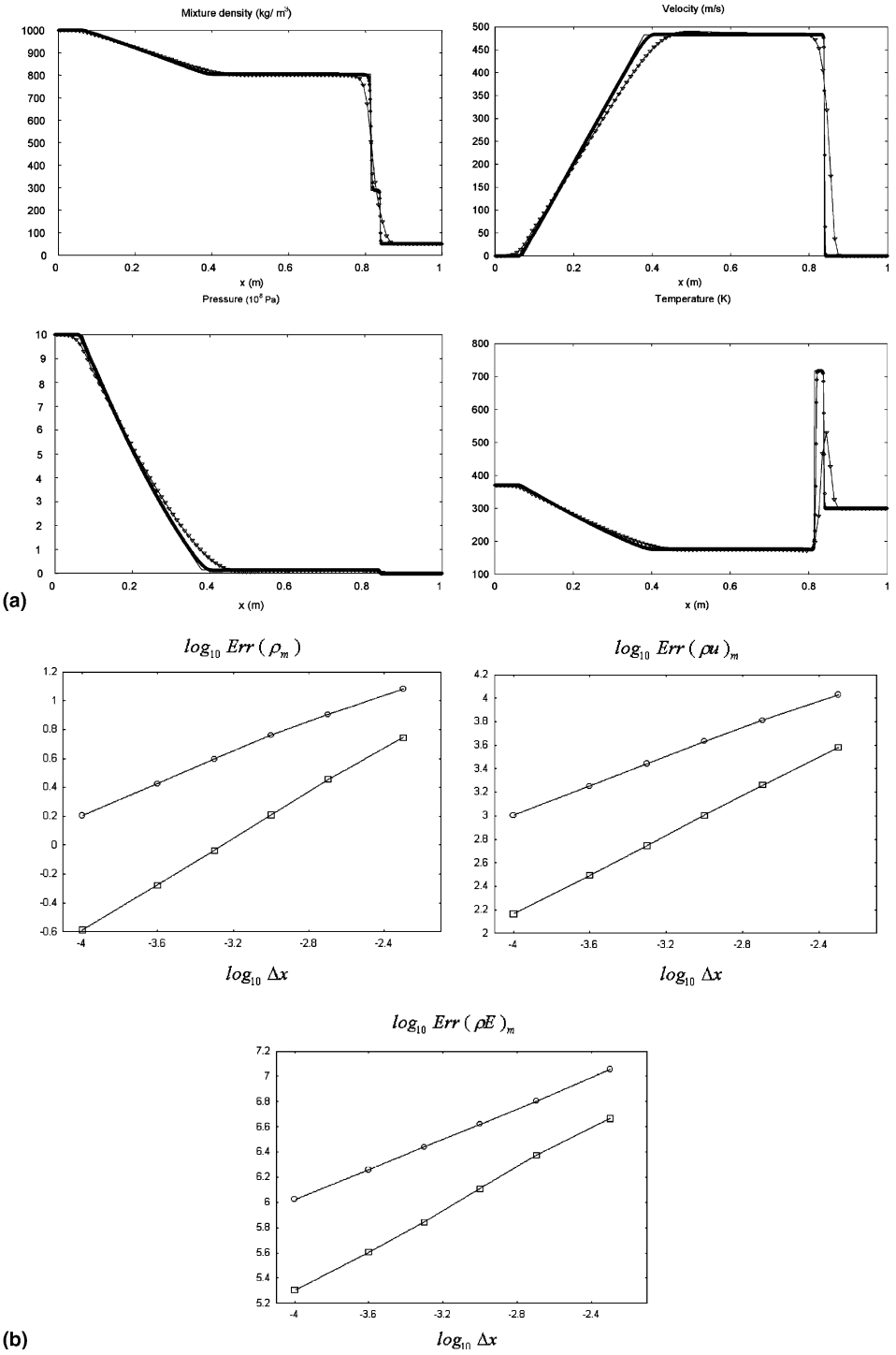

Fig. 12. (a) Exact solution (solid line), 1000 cells (circles), 100 cells (triangles). (b) Mesh convergence analysis for the shock tube test problem of (a). The lines with the circles represent the Err function associated to the first-order numerical scheme. The lines with squares are associated to the second-order variant.

small, the results with the coarse grid cannot be accurate. Computation of the temperature at the interface is not a trivial issue for interface algorithms. Most methods produce strong oscillations or do not predict the correct temperature level. This is most times related to conservation errors [29] or to convergence errors [13]. This may have serious consequences when a chemical reaction takes place at the interface, as with detonation applications. The present method predicts correctly the temperature on both sides of the interface.

We have represented in Fig. 12(b) a mesh convergence analysis for this shock tube test problem. The Err function represented corresponds to the L^1 norm for the mixture variables (density, momentum and total energy: $\rho_m = \sum(\alpha\rho)_k$, $(\rho u)_m = \sum(\alpha\rho u)_k$ and $(\rho E)_m = \sum(\alpha\rho E)_k$, respectively). It is plotted versus mesh size varying over two orders of magnitude.

The slopes of the Err function for the mixture conservative variables are approximately:

- 0.6 for the first-order numerical scheme,
- 0.75 for the second-order version.

These results are in excellent agreement with convergence analysis performed in the case of single phase Euler equations [17]. Here, the method has to deal with the presence of an interface, and converges similarly as conventional schemes used for the Euler equations.

7.2. Waves propagation in chemically inert mixtures

Before studying the propagation of linear or non-linear waves in heterogeneous reactive media, it is important to check that the multiphase model allows a correct propagation of these waves in the inert case.

Consider first the case of linear waves (i.e., acoustic waves). An asymptotic analysis of similar multiphase model has been carried out by Kapila et al. (2000) in the limit of fast pressure and velocity relaxation. They have shown that the equilibrium sound speed c_m obeys the relation:

$$\frac{1}{\rho_m c_m^2} = \sum \frac{\alpha_k}{\rho_k c_k^2} \tag{7.1}$$

with $\rho_m = \sum \alpha_k \rho_k$. This relation is known as the Wallis sound speed of the mixture and has been validated by many experiments. Thus, in the limit of fast pressure and velocity relaxation, the present model predicts correctly the propagation of acoustic wave. It is an important feature regarding detonation waves stability.

Consider now non-linear waves. The two-phase mixture does not admit conventional Rankine–Hugoniot relations because the latter relations result from the combination of the conservative, non-conservative and relaxation terms. Thus an analytical validation is very difficult. But the two-phase shock wave model prediction can be examined by comparing the numerical Hugoniot curve with the experimental one for a given mixture. Solid alloys mixtures are well documented in the literature [28]. Such mixtures are quite representative of a frozen sample of solid–gas mixtures as those produced into the reaction zone of a condensed explosive.

We consider a mixture of solid phases under piston impact. The piston impact is treated here as a boundary condition. The computed solutions are compared with experimental Hugoniot curves for solid alloys [28]. These experimental data relate the shock velocity U_s to the shocked material velocity $U_p : U_s = c_0 + sU_p$ where c_0 and s are fit on the experimental Hugoniot curve. Under very strong impact conditions, the solids are compressible and behave as fluids. In these conditions, the solid alloy can be considered as a multiphase mixture. So we compute the numerical Hugoniot curve of the alloy with the multiphase model. The multiphase model only needs the pure material equation of state. Each material is governed by the Stiffened Gas equation of state with appropriate parameters given in Table 4. Two different alloys are considered: The first is composed of epoxy and spinel. The second one is brass composed of copper and zinc.

Several unsteady impact problems have been computed with different piston velocity conditions. For each 1D unsteady multiphase run, the shock velocity U_s is determined, by examining for example the

Table 4
Parameters of the EOS of the different pure fluids

	Density (kg/m^3)	γ	p_∞ (GPa)
Copper	8924	4.22	32.4
Zinc	7139	4.17	15.7
Epoxy	1185	2.94	3.2
Spinel	3622	1.62	141.0

pressure profiles at two successive instants. It is then plotted with the corresponding material velocity U_p in Fig. 13. Each point of the numerical curve corresponds to a 1D run. These numerical data are compared with the experimental Hugoniot curve. An excellent agreement can be noted between both experimental and numerical data.

The multiphase model predicts the shock propagation as a result of the pure fluid EOS and relaxation processes between the phases. In a certain sense, it builds an "appropriate mixture EOS" and is free of adjustable parameters. This test shows that the model is able to predict the hydrodynamic behaviour of an arbitrary mixture without use of any mixture equation of state: only the pure materials equations of state are necessary.

7.3. Computation of a detonation reaction zone

The ability of the multiphase model to account for chemical or mass transfers is now examined through the following 1D simulation.

The impact of a high velocity projectile onto an explosive is considered. The shock wave is transmitted to the explosive and transits to a detonation wave that propagates through the energetic material. From the shock front (Neumann spike) chemical reactions occur until the point moving at the sonic velocity in the frame of the shock (CJ point). The flow variables into the reaction zone are compared with the exact ZND solution provided in Fickett and Davis [15]. The comparison between the exact and the numerical results can be performed only in the reaction zone that corresponds to the validity domain of the ZND model.

The multiphase model involves two different phases: a solid phase (the explosive) and a gaseous phase (detonation products). In order that the ZND solution be compared with the multiphase numerical results,

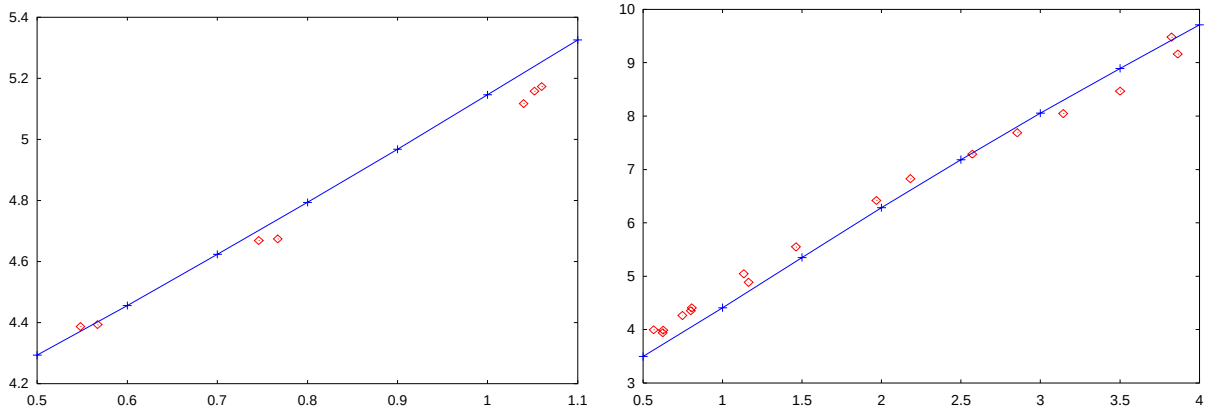

Fig. 13. U_s vs. U_p: numerical (lines) and experimental (points) shock Hugoniot curves Left: Copper–Zinc mixture (brass) with an initial zinc volume fraction of 0.29. Right: Epoxy–Spinel mixture with an initial epoxy volume fraction of 0.595.

both phases are assumed to obey the same equation of state that is to say the ideal gas law, $p = (\gamma - 1)\rho e$, with a polytropic coefficient γ equal to 3.

In this specific case, the mass transfer terms for the reactive material are:

$$\mathrm{Mass}_{\mathrm{explo}}(\alpha W) = \left(\dot{m}_{\mathrm{explo}}/\rho_{\mathrm{explo}}, \dot{m}_{\mathrm{explo}}, \dot{m}_{\mathrm{explo}}u_{\mathrm{explo}}, \dot{m}_{\mathrm{explo}}E_{\mathrm{explo}}\right)$$

and for the detonation products: $\mathrm{Mass}_{\mathrm{prod}}(\alpha W) = -\mathrm{Mass}_{\mathrm{explo}}(\alpha W)$.

The term q_{react} is the value of the combustion heat release: $q_{\mathrm{react}} = 4.5156$ MJ/kg. The mass transfer is given by $\dot{m}_{\mathrm{explo}} = -k\sqrt{(\rho_{\mathrm{m}}\alpha_{\mathrm{explo}}\rho_{\mathrm{explo}})}$ with $k = 2.10^6$ s^{-1} and $\rho_{\mathrm{m}} = \sum \alpha_k \rho_k$ is the mixture density.

Initially, the pressure is set at 1 bar and the densities of both phases are equal to 1600 kg/m^3. The computational domain is filled with the solid phase. But because of the multiphase feature of the model, a small amount of the gaseous product is also present, with a volume fraction $\alpha_{\min} = 10^{-6}$. The piston velocity is 1000 m/s.

The total length of the domain is 0.3 m. One thousand cells are used, with a constant length (3.3 cells/mm). For convenience, the time step is constant and equal to 2.33×10^{-8} s. The numerical solutions are plotted after 1400 time steps.

From the unsteady calculation the numerical velocity of the detonation front (8486 m/s) is compared with the analytical one, i.e., 8500 m/s. From a magnified view of Fig. 14, not depicted here, the measured reaction length is 5.2×10^{-3} m while the exact one is 5.3×10^{-3} m.

In Fig. 14, the numerical pressure and velocity are plotted with solid lines while the exact solution in the reaction zone is plotted with symbols. The Neumann spike and the Chapman–Jouguet point are well captured by the numerical method. The numerical solution (lines) converges to the exact one (symbols) in the reaction zone. This good agreement is also observed for the mixture density in Fig. 15.

In Fig. 15, the phases density is also plotted. Some spurious oscillations are visible around $x = 0.03$ m. They are due to the well-known overheating problem [13]. For the present test, these oscillations have no consequence on the calculation of the reaction zone. This test shows that the fluid densities are not in equilibrium. This is not surprising the combustion releases energy to the gas, increasing its temperature. As the fluids are in pressure equilibrium and out of equilibrium for the temperatures, they must have different densities. This remark also shows that the use of a thermodynamic equilibrium assumption for the building of a mixture equation of state in the context of the reactive Euler equations may lead to large errors.

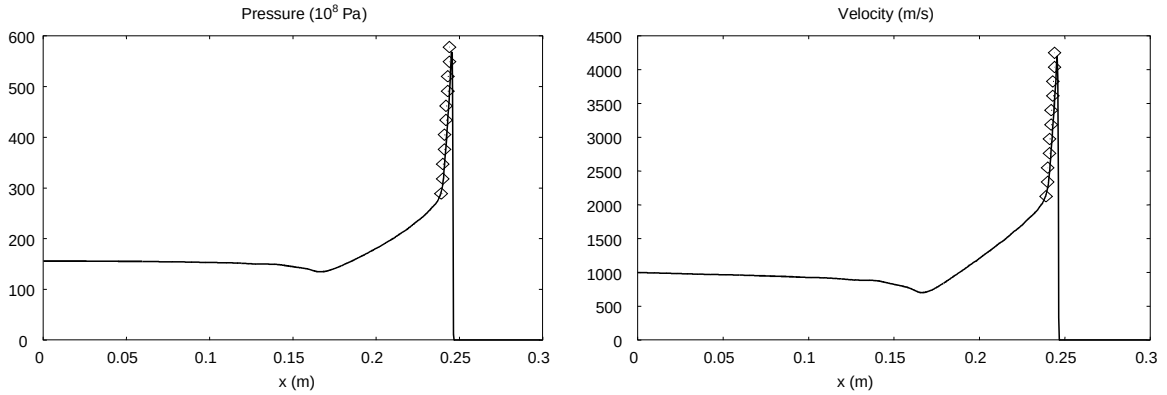

Fig. 14. Comparison of computed pressure and velocity profiles for a self-sustained detonation waves with the exact solution of the ZND problem.

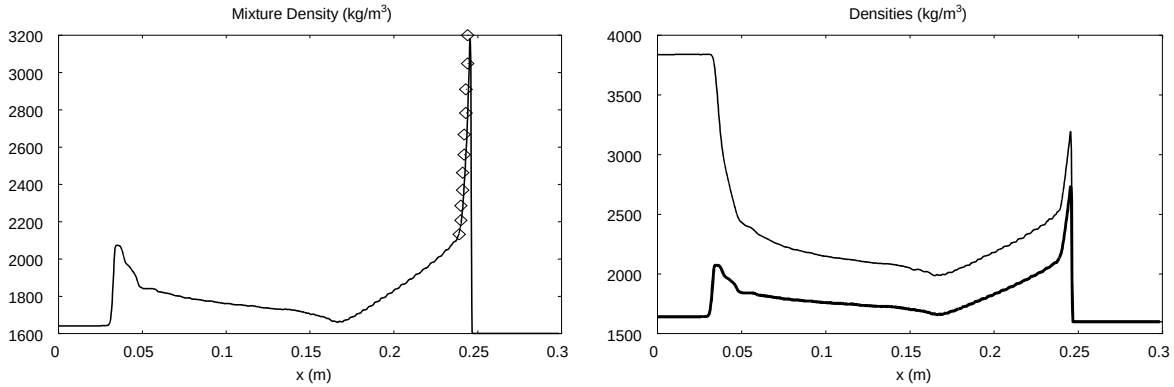

Fig. 15. Comparison of computed mixture density for a self-sustained detonation waves with the exact solution of the ZND problem. The computed phases densities are also shown.

7.4. Detonation wave in a condensed energetic material

The multiphase model is used to predict the detonation properties of a multicomponent condensed energetic material through a one-dimensional simulation. This material is initially a mixture of different chemical compounds: CHNO, ammonium perchlorate (AP) and aluminum particles. The complete decomposition chemical scheme is summarized hereafter:

$$\mathrm{C}_a\mathrm{H}_b\mathrm{N}_c\mathrm{O}_d \rightarrow \frac{c}{2}\mathrm{N}_2 + d\mathrm{H}_2\mathrm{O} + \left(\frac{b}{2} - d\right)\mathrm{H}_2 + a\mathrm{C}, \tag{R1}$$

$$\mathrm{NH}_4\mathrm{ClO}_4 \rightarrow 1.5\mathrm{H}_2\mathrm{O} + 0.5\mathrm{N}_2 + 1.25\mathrm{O}_2 + \mathrm{HCl}, \tag{R2}$$

$$\mathrm{Al} + J_3\mathrm{CO}_2 + J_3K_3\mathrm{H}_2\mathrm{O} \rightarrow 0.5\mathrm{Al}_2\mathrm{O}_3 + J_3\mathrm{C} + J_3K_3\mathrm{H}_2, \tag{R3}$$

$$\mathrm{C} + \mathrm{O}_2 \rightarrow \mathrm{CO}_2, \tag{R4}$$

$$2\mathrm{H}_2 + \mathrm{O}_2 \rightarrow 2\mathrm{H}_2\mathrm{O}. \tag{R5}$$

The molecular coefficients of the CHNO molecule are: $a = 10.83$, $b = 18.61$, $c = 5.47$, $d = 5.90$. The coefficients in the reaction (R3) are: $K_3 = 0.1$ and $J_3 = \frac{3}{2(2+K_3)}$.

This chemical scheme is due to Baudin et al. [5] and involves several reactions rates. For such type of solid–gas mixtures, the building of a mixture equation of state is not possible or not accurate as explained in the introduction. We consider each phase as a multi-component mixture governed by a mixture EOS. But the overall solid–gas mixture is treated as a separated flow.

The reactive material is governed by a multi-component Mie–Gruneisen equation of state (Appendix B) whereas the detonation gaseous products are governed by a multi-component H9 equation of state (Appendix A). Considering the jth reaction involving the ith species that can be into the condensed or gas phase, the chemical mechanism can be written in the form

$$\sum_{i=1}^{N_s+N_g} \nu'_{ij} X_i \rightarrow \sum_{i=1}^{N_s+N_g} \nu''_{ij} X_i \quad \text{for all } j = 1, \ldots, N_{\text{react}}.$$

N_s and N_g are the total amount of chemical species in solid and gaseous phase, respectively. N_{react} is the total number of chemical reactions. $[X_i]$ is the species volume concentrations of the ith component. The rate of change of the different compounds must be now modelled. The products being in a solid state, a pressure-dependent relation is generally used. Then, the time variation of the concentration is given by:

$$[\dot{X}_i] = \sum_{j=1}^{N_{react}} \frac{\nu''_{ij} - \nu'_{ij}}{\tau'_j} \left(\prod_{l=1}^{N_g+N_s} [X_l]^{\beta_l^j} \right)$$

with τ'_j is a function of the relaxed pressure:

$$\frac{1}{\tau'_j} = A_j \left(\frac{p}{p_0}\right)^n.$$

A_j, p_0 and n are parameters that depend on the jth reaction. There is no difficulty to obtain the expression of the mass transfer:

$$\dot{m}_i = \sum_{j=1}^{N_{react}} \frac{\nu''_{ij} - \nu'_{ij}}{\tau_j} \left(\prod_{ks=1}^{N_s} \left((\alpha\rho)_s Y_{ks}\right)^{\beta_{ks}^j} \prod_{kg=1}^{N_g} \left((\alpha\rho)_g Y_{kg}\right)^{\beta_{kg}^j} \right)$$

The values of the different parameters can be found in Baudin et al. [6]. They are summarized in Table 5:

In the computations, the condensed explosive has the initial density of 1800 kg/m^3 and is impacted by a projectile at a velocity equal to 400 m/s. The multiphase model necessitates that initially a small amount of gas exists in the computational domain. We suppose that some gaseous water is present with an initial gas volume fraction of 10^{-3}. The explosive is initially at rest under atmospheric conditions.

The length of the domain is equal to 1 m. The number of numerical cells is equal to 1000. The time step is equal to 0.5 CFL.

Table 5
Kinetic parameters of the chemical scheme (R1)–(R5)

Reaction index j	A_j (s^{-1})	Reaction order β^j
1	1×10^5	$\beta_{CHNO} = 1$
2	0.085×10^5	$\beta_{NH_4ClO_4} = 1$
3	0.075×10^5	$\beta_{Al} = 1, \beta_{H_2O} = 1, \beta_{CO_2} = 1$
4	1×10^5	$\beta_C = 1, \beta_{O_2} = 1$
5	1×10^5	$\beta_{H_2} = 1, \beta_{O_2} = 1/2$

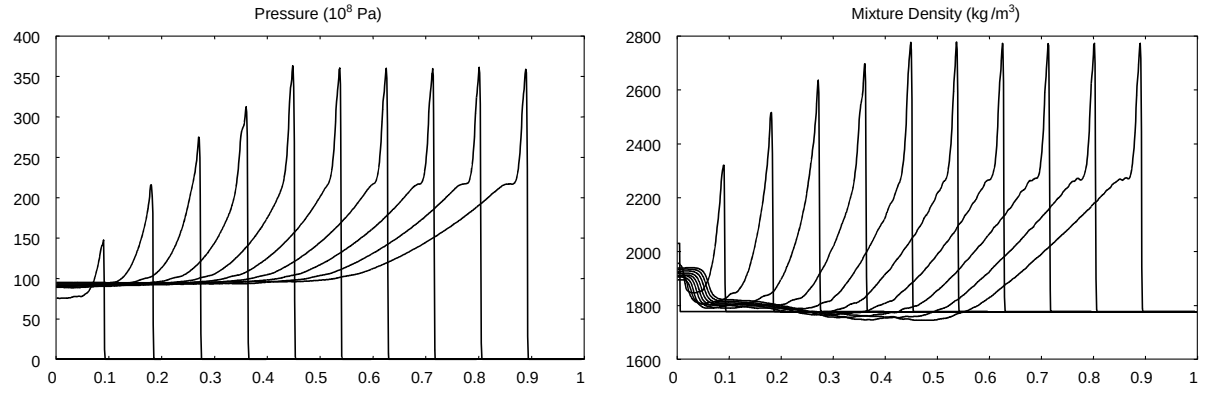

Fig. 16. Pressure and mixture density profiles at different times.

In Fig. 16, the pressure and the mixture density profiles are plotted for different times. The stable detonation wave is obtained at $x = 0.7$ m.

The specificity of the chemical composition leads to a partial decomposition of the reactants. In Fig. 17, profiles of solid and gaseous phase volume fraction are plotted when the detonation wave is stable. Upstream the CJ point, there is a two-phase mixture made of around 30% of gas and 70% of solid: this point also shows that a multiphase description is necessary.

With the multiphase model proposed, the composition of each phase is accurately determined. In Fig. 18, the different mass fraction profiles of the chemical species in each phase are plotted. A magnified view of the reaction zone is presented. In the solid phase, three characteristics times associated to three chemical reactions can clearly be seen. The CHNO decomposition is very fast and complete. This reaction produces the necessary chemical species as well as the pressure and temperature conditions to initiate the two other reactions. The entire AP burns on a larger timescale. On the contrary, the aluminium is not totally burnt and the final solid mixture is made of aluminium and its oxide. The evolutions of the various species clearly show that a thermodynamic equilibrium computation and the derivation of reduced equation of state for the gas phase, as well as for the condensed is not possible. It is the reason why theoretical equations of state are used (Appendices A and B). Their use necessitates the determination of the various

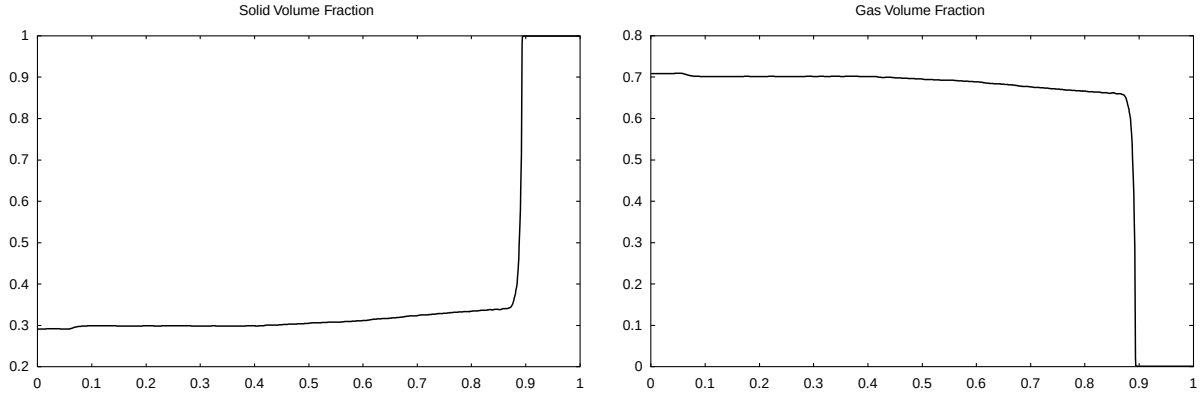

Fig. 17. Solid and gas volume fraction.

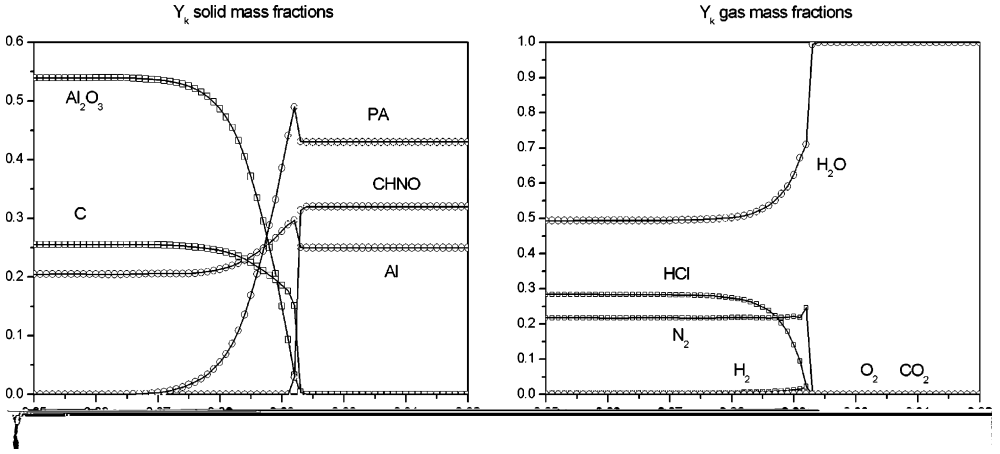

Fig. 18. Mass fractions of the solid and of the gaseous products.

species concentrations as well as the thermodynamic variables in each phase. This justifies the use of the multiphase model.

7.5. Two-dimensional detonation simulation

In this section, a two-dimensional simulation is presented and shows the ability of the model to predict the behaviour of practical systems. A projectile moving in the air impacts a tank made in copper, containing a liquid explosive (nitromethane). The detonation propagation will increase the pressure in the tank until complete destruction. A schematic view of the system is presented in Fig. 19. In addition to the propagation of the detonation wave, some specific problems appear: they are related to the contact/material interfaces, traction/cavitation of solids, temperature dependence of the chemical mechanism. These phenomena are to be involved in the model.

Four different phases (and as many EOS) are necessary for the present computation: one for the air (ideal gas), one for the copper (stiffened gas), one for the liquid NM [11] and the fourth for the gaseous detonation products (JWL, [26]). All equations of state and chemical kinetic parameters are provided in Baudin et al. [7] following the experimental facility and methods presented in Serradeill et al. [35].

The initial conditions correspond to a system at standard conditions, only the projectile has a velocity equal to 1930 m/s. The volume fraction of each phase is at least equal to 10^{-4} if it is a minor one at the location considered, about one otherwise.

The physical length of the domain is 78×10^{-3} m, and the half-height is 50×10^{-3} m. The mesh used here is a 100×50 cells and the total CPU time is about 5 h on a 2 GHz PC. The time step is restricted to 0.2 CFL because of the chemical stiffened of the Arrhenius laws of nitromethane. In Fig. 20, the mesh is shown. The mixture density seems to be the more pertinent quantity to appreciate the different steps of the overall phenomenon. Its evolution is depicted in Fig. 20.

In Fig. 20(a), the initial mixture density is plotted and one can easily recognize the wall tank and the projectile. In the next view, the moving projectile has penetrated the envelope, which is deforming. The initial shock wave is now transmitted to the liquid explosive. In Fig. 20(c), a curved detonation wave is observed which propagates in the liquid. One can also see in this figure, that a very low-pressure zone inside the projectile. This is due to the 2D rarefactions wave that reflects from the free boundaries of the projectile. Focusing of this wave onto the axis leads to an expansion/traction of the copper as it is described in Thouvenin [38]. In Fig. 20(d), the detonation wave has reached the upper wall. This interaction has amplified the front curvature: lateral expansions induce front curvature. It is noticeable that the left wall above the projectile has a motion toward the left: it is due to the pressure difference between the inside and the outside of the tank.

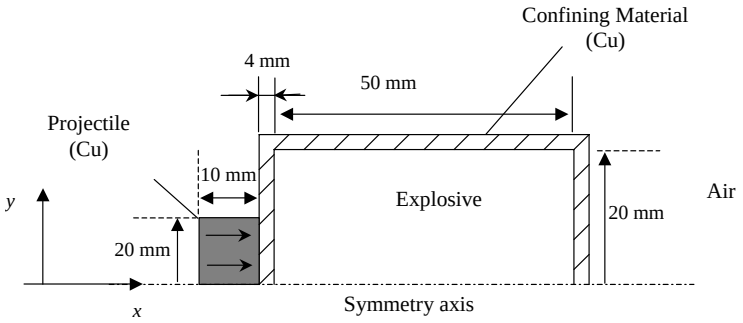

Fig. 19. Presentation of the system simulated by a two-dimensional calculation.

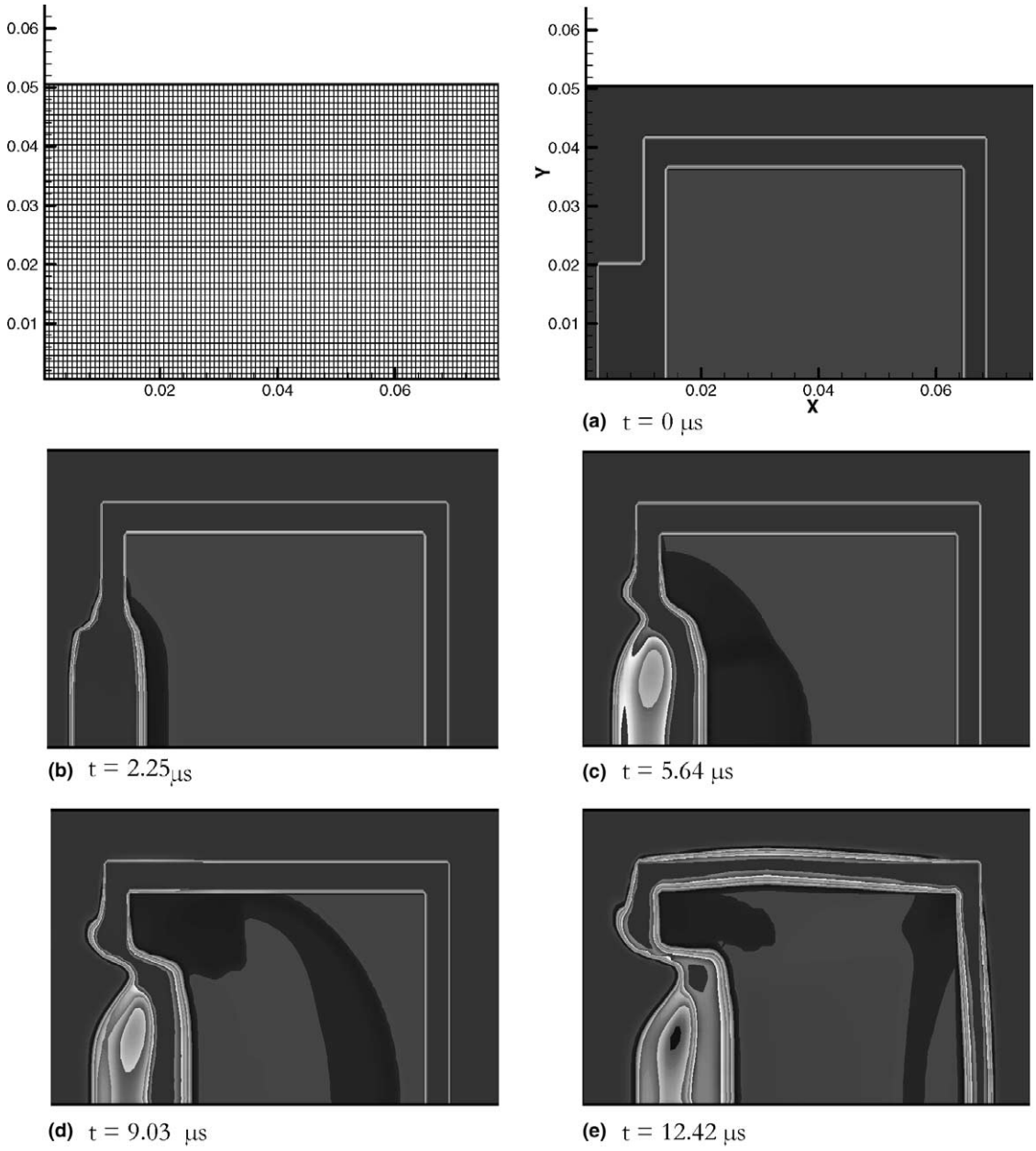

Fig. 20. Grid and evolution of the mixture density in the two-dimensional case.

8. Conclusion

Two important issues have been addressed in the present paper:

- the computation of macroscopic material interfaces and,
- the thermodynamic modelling of condensed explosives.

These two challenging problems have been solved with a generalized multiphase model and resolution method. It was important to consider these issues in a general framework since the detonation dynamics is always coupled with surrounding materials through their interactions at material interfaces. To succeed in this task, the discrete equations method (DEM) of Abgrall and Saurel [2] has been the subject of important extensions:

- The averaging method has been revisited and re-interpreted in terms of geometrical averages only. No stochastic average is used.
- The flow topology has been chosen as representative of the granular mixture. By deriving the discrete model for such topology a model be valid for material interfaces as well as for packed solid granular beds has been obtained. The continuous limit of this discrete model has also been determined and analysed. It has provided relaxation coefficients that generalize the conventional formulas. These coefficients prove that the model is suited to fluid mixtures evolving essentially under a single velocity and pressure, in the context of the very high pressure conditions of detonation physics. The same analysis provides estimates for the interface pressure and velocity. The resulting thermo-mechanical model is closed and is free of parameter.
- The multiphase hydrodynamic model, used for detonation wave propagation is free of mixture equation of state. Only the pure materials equation of state are necessary. They require the solid and gas chemical compositions, that are determined.
- The model is shown to obey a dissipative inequality.
- Applications involving detonations in condensed material involve several fluids: the condensed phase, the gas products, a solid or liquid phase representing the surrounding material, the ambient air. Our strategy is to solve the same equations everywhere, with the same numerical method. In this context, the model needs to be extended to an arbitrary number of fluids. Both model and numerical method have been extended in this direction.
- The method has been extended to 2D and several validation problems have been examined.

The main perspective of this work is to model micro-structural effects that occur during shock initiation of condensed energetic materials. When a shock wave propagates through a granular material, part of the energy is focused into micro-structural defects and the micro-mechanical motion accompanied with dissipation at the same scale forms so called "hot spots". Modelling the effects at this scale poses difficulties, as well as the coupling between micro-scale events to the wave dynamics at the macro-scale. This topic has been addressed in Massoni et al. (1999). The macroscopic model was composed of the mixture Euler equations and the microscopic one was based on visco-plastic pore collapse equations. The macroscopic model could be improved by employing the approach developed herein. Such issue has been addressed by Gavrilyuk and Saurel [18] in the simplified situation of non-reacting bubbly liquids.

Appendix A. The multi-component H9 equation of state for the gas products

The H9 equation of state is a multi-component equation of state used to describe gaseous detonation products. It is a fifth-order virial expansion, specifically developed for detonation of CHNO-type explosives. The pressure is given by

$$P_{\mathrm{g}} = \frac{R}{M_{\mathrm{g}}}\rho_{\mathrm{g}} T_{\mathrm{g}} \sigma(x),$$

where $x = \Omega \rho_{\mathrm{g}} T_{\mathrm{g}}^{-1/3}$ and $\Omega = k \sum_{kg=1,\ldots,N_{\mathrm{g}}} \frac{Y_{kg}}{M_{kg}} l_{kg}$ and $\sigma(x)$ is a fifth-order polynomial.In these expressions, Y_{kg}, M_{kg} and l_{kg} are the mass fraction, the molar mass and the covolume of the kgth gaseous species, k is an adjustable parameter ($k = 63.5 \times 10^{-6}$ mol/m^3), R the Avogrado constant ($R = 8.314$ J/K mol) and M_{g} the molar of the gas mixture.

The internal energy is given by:

$$e_{\mathrm{g}} = e_{\mathrm{g},0}(Z) + \frac{R}{M_{\mathrm{g}}} T_{\mathrm{g}} \frac{\sigma(x) - 1}{3},$$

where $e_{\mathrm{g},0}(Z) = \sum_{kg} Y_{kg}(a_{kg}Z^2 + b_{kg}Z + c_{kg})$ and

$$Z = \begin{cases} T_{\mathrm{g}} & \text{if } T_{\mathrm{g}} \leqslant 1200 \text{ K}, \\ T_{\mathrm{g}}\left(1 + 2\frac{\ln(T_{\mathrm{g}}/1200)}{\ln P_{\mathrm{g}}}\right) & \text{if } T_{\mathrm{g}} > 1200 \text{ K} \end{cases}$$

The $\{a_{kg}, b_{kg}, c_{kg}\}_{kg=1,\ldots,N_{\mathrm{g}}}$ are fitted coefficients [20].

The sound speed of the H9 equation of state is given by

$$c_{\mathrm{g}}^2 = \left.\frac{\mathrm{d}P_{\mathrm{g}}}{\mathrm{d}\rho_{\mathrm{g}}}\right|_{\eta_{\mathrm{g}}, Y_{kg}}, \quad \text{i.e.,} \quad c_{\mathrm{g}}^2 = \left.\frac{\partial P_{\mathrm{g}}}{\partial \rho_{\mathrm{g}}}\right|_{T_{\mathrm{g}}, Y_{kg}} + \left.\frac{\partial P_{\mathrm{g}}}{\partial T_{\mathrm{g}}}\right|_{\rho_{\mathrm{g}}, Y_{kg}} \frac{\dfrac{P_{\mathrm{g}}}{\rho_{\mathrm{g}}^2} - \left.\dfrac{\partial e_{\mathrm{g}}}{\partial \rho_{\mathrm{g}}}\right|_{T_{\mathrm{g}}, Y_{kg}}}{\left.\dfrac{\partial e_{\mathrm{g}}}{\partial T_{\mathrm{g}}}\right|_{\rho_{\mathrm{g}}, Y_{kg}}}.$$

Appendix B. Multi-component Mie–Gruneisen equation of state for the solid reactant

A multi-component equation of state has been built in order to reproduce the behaviour of heterogeneous condensed materials under shock waves from the various thermodynamic parameters of the various components.

The equation of state can be written under the following form:

$$e_{\mathrm{s}} = e_{\mathrm{s}}^0 + C_{\mathrm{v}} T_{\mathrm{s}} \quad \text{and} \quad P_{\mathrm{s}} = P_{\mathrm{s}}^0 + (\Gamma \rho_{\mathrm{s}}) C_{\mathrm{v}} T_{\mathrm{s}},$$

where $\Gamma = \Gamma(\{Y_{ks}\})$ is the Gruneisen coefficient and $C_{\mathrm{v}} = \sum_{ks} Y_{ks} C_{v,ks}$ the specific heat at constant volume of the multi-component solid and $C_{v,ks}$ is the specific heat at constant volume of the ksth component of the solid.

The first part of the internal energy e_{s}^0 is given by the relation

$$e_{\mathrm{s}}^0 = e_{\mathrm{s1}}^0(\rho, \{Y_{ks}\}) + e_{\mathrm{s2}}^0(\rho, \{Y_{ks}\})$$

with $e_{\mathrm{s1}}^0(\rho, \{Y_{ks}\}) = \sum_{ks} Y_{ks} e_{ks}^0 + Q(\rho, \{Y_{ks}\})$, Q is a rational quotient function of the solid density and of its mass fraction. The second function reads $e_{\mathrm{s2}}^0(\rho, \{Y_{ks}\}) = -C_{\mathrm{v}} T_0 \exp(\Gamma x(\rho))$ with $x(\rho) = \frac{\rho - \rho_0}{\rho}$.

The pressure P_{s}^0 is defined by $P_{\mathrm{s}}^0 = P_{\mathrm{s1}}^0 + P_{\mathrm{s2}}^0$ with

$$P_{\mathrm{s1}}^0 = -\left.\frac{\partial e_{\mathrm{s1}}^0}{\partial(1/\rho)}\right|_{Y_{ks}} \quad \text{and} \quad P_{\mathrm{s2}}^0 = -\left.\frac{\partial e_{\mathrm{s2}}^0}{\partial(1/\rho)}\right|_{Y_{ks}}.$$

The sound speed for the multi-component solid is therefore

$$c_{\mathrm{s}}^2 = \left.\frac{\mathrm{d}P_{\mathrm{s}}}{\mathrm{d}\rho_{\mathrm{s}}}\right|_{\eta_{\mathrm{s}}, Y_{ks}} = \frac{\dfrac{P_{\mathrm{s}}}{\rho_{\mathrm{s}}^2} - \left.\dfrac{\partial e_{\mathrm{s}}}{\partial \rho_{\mathrm{s}}}\right|_{P_{\mathrm{s}}, Y_{ks}}}{\left.\dfrac{\partial e_{\mathrm{s}}}{\partial P_{\mathrm{s}}}\right|_{\rho_{\mathrm{s}}, Y_{ks}}}.$$

Appendix C. Determination of the contacts surfaces at the cells boundaries for an arbitrary number of fluids

We have developed in Section 3 and summarized in Tables 1 and 2 the calculation method for the contact surfaces at the cells boundaries for mixtures involving two phases only. We now develop the calculation procedure in the case of a multiphase mixture.

At a given cell boundary each fluid occupies on the right and left sides a fraction of the cross section. We denote this surface fraction $S_{k,\mathrm{R}}$ and $S_{k,\mathrm{L}}$, where the index k represents the phase and the subscripts R and L the right and left sides respectively, relative to the cell boundary.

These surface fractions are defined by: $S_{k,\mathrm{R}} = \bar{X}_k = \frac{1}{\Delta y}\int_0^{\Delta y} X_k \,\mathrm{d}y$.

In the following procedure, these surface fractions are assumed equal to the volume fractions: $S_k = \alpha_k$.

Let us first examine the particular case of two phases first. The method proceed as a recurrence process in which the initial data corresponds to the left and right surface fractions with respect to the cell boundary ($i - 1/2$ in this example):

$$S^{(0)}_{1,\mathrm{L}} = \alpha_{1,i-1}, \quad S^{(0)}_{1,\mathrm{R}} = \alpha_{1,i},$$
$$S^{(0)}_{2,\mathrm{L}} = \alpha_{2,i-1}, \quad S^{(0)}_{2,\mathrm{R}} = \alpha_{2,i}$$

The superscript (0) represents the initial state of the recurrence procedure. To proceed to the next step, some kind of continuity assumption has to be formulated in each phase. We assume that each phase has the maximum possible contact surface with itself. This maximum contact surface cannot exceed the smallest of the two surfaces of a given phase present at the cell boundary. This assumption provides the first two contact surfaces at the cell boundary:

$$S_{11} = \min(S^{(0)}_{1,\mathrm{L}}, S^{(0)}_{1,\mathrm{R}}) \quad \text{and} \quad S_{22} = \min(S^{(0)}_{2,\mathrm{L}}, S^{(0)}_{2,\mathrm{R}}).$$

From this result, the remaining available surfaces on the right and left sides of the cell boundary are readily obtained. It determines the next step of the recurrence formula:

$$S^{(1)}_{1,\mathrm{L}} = S^{(0)}_{1,L} - S_{11}, \quad S^{(1)}_{1,\mathrm{R}} = S^{(0)}_{1,\mathrm{R}} - S_{11},$$
$$S^{(1)}_{2,\mathrm{L}} = S^{(0)}_{2,\mathrm{L}} - S_{22}, \quad S^{(1)}_{2,\mathrm{R}} = S^{(0)}_{2,\mathrm{R}} - S_{22}.$$

The contact between two surfaces will occur necessary with the smallest of the two remaining surfaces: $S_{12} = \min(S^{(1)}_{1,\mathrm{L}}, S^{(1)}_{2,\mathrm{R}})$ and $S_{21} = \min(S^{(1)}_{2,\mathrm{L}}, S^{(1)}_{1,\mathrm{R}})$.

These results are summarized in Table 6:

It can be easily checked that $S_{11} + S_{12} + S_{21} + S_{22} = 1$ as well as $S_{11} + S_{12} = \alpha_{1,i-1}$, $S_{11} + S_{12} = \alpha_{1,i-1}$, $S_{11} + S_{21} = \alpha_{1,i}$ and $S_{22} + S_{12} = \alpha_{2,i}$. These results are the same as the ones proposed initially in Table 2.

We now examine the case with three phases. As previously the initial data corresponds to the left and right surface fractions with respect to the cell boundary:

$$S^{(0)}_{1,\mathrm{L}} = \alpha_{1,i-1}, \quad S^{(0)}_{1,\mathrm{R}} = \alpha_{1,i},$$
$$S^{(0)}_{2,\mathrm{L}} = \alpha_{2,i-1}, \quad S^{(0)}_{2,\mathrm{R}} = \alpha_{2,i},$$
$$S^{(0)}_{3,\mathrm{L}} = \alpha_{3,i-1}, \quad S^{(0)}_{3,\mathrm{R}} = \alpha_{3,i}.$$

With the help of the continuity assumption we get:

$$S_{11} = \min(S^{(0)}_{1,\mathrm{L}}, S^{(0)}_{1,\mathrm{R}}), \qquad S_{22} = \min(S^{(0)}_{2,\mathrm{L}}, S^{(0)}_{2,\mathrm{R}}), \qquad S_{33} = \min(S^{(0)}_{3,\mathrm{L}}, S^{(0)}_{3,\mathrm{R}}).$$

From which we determine the remaining surfaces:

$$S^{(1)}_{1,\mathrm{L}} = S^{(0)}_{1,\mathrm{L}} - S_{11}, \quad S^{(1)}_{1,\mathrm{R}} = S^{(0)}_{1,\mathrm{R}} - S_{11},$$
$$S^{(1)}_{2,\mathrm{L}} = S^{(0)}_{2,\mathrm{L}} - S_{22}, \quad S^{(1)}_{2,\mathrm{R}} = S^{(0)}_{2,\mathrm{R}} - S_{22},$$
$$S^{(1)}_{3,\mathrm{L}} = S^{(0)}_{3,\mathrm{L}} - S_{33}, \quad S^{(1)}_{3,\mathrm{R}} = S^{(0)}_{3,\mathrm{R}} - S_{33}.$$

Table 6
Contact surfaces at cell boundary $(i-1/2)$ for a two-phase mixture

Contact type	Contact surface
1–1	$S_{11} = \min(\alpha_{1,i-1}, \alpha_{1,i})$
1–2	$S_{12} = \min(\alpha_{1,i-1} - S_{11}, \alpha_{2,i} - S_{22})$
2–1	$S_{21} = \min(\alpha_{1,i} - S_{11}, \alpha_{2,i-1} - S_{22})$
2–2	$S_{22} = \min(\alpha_{2,i-1}\alpha_{2,i})$

We now need another assumption associated with the mixture topology. A ''priority'' has to be defined for the contact of the various phases. Imagine that phase 1 is the solid reacting phase, phase 2 its reaction product and phase 3 an inert phase. It is legitimate to give a priority to contact between the solid phase and its reaction products. But the contact surface between these two phases cannot exceed the smallest of the two surfaces present at the cell boundary. Thus,

$$S_{12} = \min(S_{1,\mathrm{L}}^{(1)}, S_{2,\mathrm{R}}^{(1)}) \quad \text{and} \quad S_{21} = \min(S_{2,\mathrm{L}}^{(1)}, S_{1,\mathrm{R}}^{(1)}).$$

We then deduce:

$$\begin{aligned}
&S_{1,\mathrm{L}}^{(2)} = S_{1,\mathrm{L}}^{(1)} - S_{12}, \quad S_{1,\mathrm{R}}^{(2)} = S_{1,\mathrm{R}}^{(1)} - S_{21},\\
&S_{2,\mathrm{L}}^{(2)} = S_{2,\mathrm{L}}^{(1)} - S_{21}, \quad S_{2,\mathrm{R}}^{(2)} = S_{2,\mathrm{R}}^{(0)} - S_{12},\\
&S_{3,\mathrm{L}}^{(2)} = S_{3,\mathrm{L}}^{(1)}, \quad S_{3,\mathrm{R}}^{(2)} = S_{3,\mathrm{R}}^{(1)}.
\end{aligned}$$

From which the remaining contact surfaces are deduced: $S_{13} = \min(S_{1,\mathrm{L}}^{(2)}, S_{3,\mathrm{R}}^{(2)})$, $S_{23} = \min(S_{2,\mathrm{L}}^{(2)}, S_{3,\mathrm{R}}^{(2)})$, $S_{31} = \min(S_{3,\mathrm{L}}^{(2)}, S_{1,\mathrm{R}}^{(2)})$, $S_{32} = \min(S_{3,\mathrm{L}}^{(2)}, S_{2,\mathrm{R}}^{(2)})$. These results are summarized in Table 7.

This procedures shows certain degrees of freedom for the choice of these contact surfaces, provided that the various saturation constraints be fulfilled.

Table 7 gives an example when the contact of the phases with themselves is the first priority, and when the contact between the reactive material and its products is the second priority.

From this observations, a general recurrence procedure can be proposed. It necessitates the definition of contact priorities at each step m of the recurrence process between two phases: phase k and its priority phase p_k^m during step m.

Example: Preceding system with 3 phases.

$$m = 0, \quad p_1^0 = 1, \quad p_2^0 = 2 \quad \text{and} \quad p_3^0 = 3$$

Table 7
Contact surfaces at cell boundary $(i-1/2)$ for a mixture with three phases: phase 1 is a reactive material, phase 2 its reaction products and phase 3 an inert material

Contact type	Contact surface
1–1	$S_{11} = \min(\alpha_{1,i-1}, \alpha_{1,i})$
1–2	$S_{12} = \min(\alpha_{1,i-1} - S_{11}, \alpha_{2,i} - S_{22})$
2–1	$S_{21} = \min(\alpha_{1,i} - S_{11}, \alpha_{2,i-1} - S_{22})$
2–2	$S_{22} = \min(\alpha_{2,i-1}, \alpha_{2,i})$
1–3	$S_{13} = \min(\alpha_{1,i-1} - S_{11} - S_{12}, \alpha_{3,i} - S_{33})$
2–3	$S_{23} = \min(\alpha_{2,i-1} - S_{22} - S_{21}, \alpha_{3,i} - S_{33})$
3–1	$S_{31} = \min(\alpha_{3,i-1} - S_{33}, \alpha_{1,i} - S_{11} - S_{21})$
3–2	$S_{32} = \min(\alpha_{3,i-1} - S_{33}, \alpha_{2,i} - S_{22} - S_{12})$
3–3	$S_{33} = \min(\alpha_{3,i}, \alpha_{3,i-1})$

$$m = 1, \quad p_1^1 = 2,$$

$$m = 2, \quad p_1^2 = 3 \quad \text{and} \quad p_2^2 = 3.$$

From these priorities, the contact surfaces at the cell boundary are computed at each step by the formulae: $S_{k,p_k^m} = \min(S_{k,L}^m, S_{p_k^m,R}^m)$ and $S_{p_k^m,k} = \min(S_{p_k^m,L}^m, S_{k,R}^m)$.

The remaining surfaces at the next step of the recurrence procedure are obtained by:

$$S_{k,\mathrm{L}}^{m+1} = S_{k,\mathrm{L}}^m - S_{k,p_k^m} \quad \text{and} \quad S_{k,\mathrm{R}}^{m+1} = S_{k,\mathrm{R}}^m - S_{p_k^m,k}.$$

It must be checked at the last step ($m = 2$ here) that all $S_{k,\mathrm{L}}^{m+1}$ and $S_{k,\mathrm{R}}^{m+1}$ are zero.

References

[1] R. Abgrall, How to prevent pressure oscillations in multicomponent flows: a quasi-conservative approach, J. Comput. Phys. 125 (1996) 150–160.

[2] R. Abgrall, R. Saurel, Discrete equations for physical and numerical compressible multiphase mixtures, J. Comput. Phys. 186 (2) (2003) 361–396.

[3] M.R. Baer, J.W. Nunziato, A two-phase mixture theory for the deflagration-to-detonation transition in reactive granular materials, Int. J. Multiphase Flows 12 (1986) 861–889.

[4] G. Baudin, Un code thermochimique adapté au calcul des caractéristiques de détonation des explosifs aluminisés. Europyro 1993, Strasbourg, 1993, pp. 409–418 (in French).

[5] G. Baudin, M. Cauret, Y. Lagarde, Modélisation du comportement détonique d'explosifs de type CHNO, Rapport du Centre d'Etudes de Gramat, 1999 (in French).

[6] B. Baudin, Détonation, in: 5th Summer School CNRS-SFT 26th June–1st July 2000, Porquerolles, France (Edited by Ecole Polytechnique de Marseille, Université de Provence, France, 2000 (in French)).

[7] G. Baudin, C. Le Gallic, R. Serradeill, Amorçage par choc et détonation du nitrométhane. Partie 2 – Modélisation et simulation numérique des mécanismes réactifs, in: Fifth International Symposium of High Dynamic Pressures, June 23–27, Saint-Malo, France, Tome 1, 2003, pp. 241–254 (in French).

[8] D.J. Benson, Computational methods in Lagrangian and Eulerian hydrocodes, Comput. Meth. Appl. Mech. Eng. 99 (1992) 235–394.

[9] P.B. Butler, M.F. Lambeck, H. Krier, Modeling of shock development and transition to detonation initiated by burning in porous propellants beds, Combust. Flame 46 (1982) 75–93.

[10] A. Chorin, Random choice methods with applications to reacting gas flows, J. Comput. Phys. 25 (1977) 253–272.

[11] G. Cochan, J. Chan, Shock initiation and detonation models in one and two dimensions, Lawrence National Laboratory report, 1979.

[12] D.A. Drew, S.L. Passman, Theory of multicomponent fluids, in: Applied Mathematical Sciences, vol. 135, Springer, New York, 1998.

[13] R. Fedkiw, A. Marquina, B. Merriman, An isobaric fix for the overheating problem in multimaterial compressible flows, J. Comput. Phys. 148 (2) (1999) 545–578.

[14] R. Fedkiw, T. Aslam, B. Merriman, S. Osher, A non-oscillatory Eulerian approach to interfaces in multimaterial flows (The Ghost Fluid Method), J. Comput. Phys. 152 (1999) 457–492.

[15] W. Fickett, W.C. Davis, Detonation, University of California Press, 1979.

[16] L.E. Fried, Cheetah 1.39 User's Manual, Lawrence Livermore National Laboratory, Energetic Materials Center, 1996.

[17] T. Gallouet, J.M. Hérard, N. Seguin, Some recent finite volume schemes to compute Euler equations using real gas EOS, Int. J. Numer. Meth. Fluids 39–12 (2002) 1073–1138.

[18] S. Gavrilyuk, R. Saurel, Mathematical and numerical modeling of two-phase compressible flows with micro-inertia, J. Comput. Phys. 175 (1) (2002) 326–360.

[19] E. Godlewski, P.A. Raviart, Numerical Approximation of Hyperbolic Systems of Conservation Laws, Springer, Berlin, 1996.

[20] O. Heuzé, Equation of state of detonation products: influence in the repulsive intermolecular potential, Phys. Rev. A 34 (1) (1986) 428–433.

[21] A.K. Kapila, S.F. Son, J.B. Bdzil, R. Menikoff, D.S. Stewart, Two-phase modelling of DDT: structure of the velocity relaxation zone, Phys. Fluids 9 (1997) 3885–3897.

[22] A.K. Kapila, R. Menikoff, J.B. Bdzil, S.F. Son, D.S. Stewart, Two-phase modelling of DDT in granular materials: reduced equations, Phys. Fluids 13 (2001) 3002–3024.

[23] S. Karni, Multicomponent flow calculations by a consistent primitive algorithm, J. Comput. Phys 112 (1994) 31–43.
[24] S. Karni, Hybrid multifluid algorithm, SIAM J. Sci. Comput. 17 (1996) 1019–1039.
[25] M.H. Lallemand, A. Chinnayya, O. LeMetayer, Pressure relaxation procedures for multiphase flows, Int. J. Numer. Meth. Fluids, in revision, 2004.
[26] E.L. Lee, H.C. Horning, J.W. Kury, Adiabatic Expansion of HIFH Explosives Detonation Products, Lawrence Radiation Laboratory, University of California, Livermore, 1968, TID 4500-UCRL 50422.
[27] O. Le Metayer, J. Massoni, R. Saurel, Modelling evaporation waves using reactive Riemann solver, in preparation, 2004.
[28] S.P. Marsh, LASL Shock Hugoniot Data, University of California Press, 1959.
[29] J. Massoni, R. Saurel, B. Nkonga, R. Abgrall, Proposition de méthodes et modèles eulériens pour les problèmes à interfaces entre fluides compressibles en présence de transfert de chaleur, Int. J. Heat Mass Transfer 45 (6) (2000) 1287–1307 (in French).
[30] D.R. Mott, E.S. Oran, B. Van Leer, New quasi-steady-state and partial equilibrium methods for integrating chemically reacting systems, J. Comput. Phys. 164 (2000) 407–428.
[31] R. Saurel, M. Larini, J.C. Loraud, Numerical modelling of deflagration–detonation transition produced by laser impact on granular explosives, Comput. Fluid Dyn. J. 1 (2) (1992) 250–261.
[32] R. Saurel, R. Abgrall, A multiphase Godunov method for compressible multifluid and multiphase flows, J. Comput. Phys. 150 (1999) 425–467.
[33] R. Saurel, R. Abgrall, A simple method for compressible multifluid flows, SIAM J. Sci. Comput. 21 (3) (1999) 1115–1145.
[34] R. Saurel, O. Le Metayer, A multiphase model for compressible flows with interfaces, shocks, detonation waves and cavitation, J. Fluid Mech. 431 (2001) 239.
[35] R. Serradeill, C. Le Gallic, P. Bouinot, G. Baudin, Shock ignition and detonation of nitromethane – Part 1: experimental determination of reactive mechanisms, in: Fifth International Symposium High Dynamic Pressures, June 23–27, Saint-Malo, France, Tome 1, 2003, pp. 155–166.
[36] K.-M. Shyue, An efficient shock-capturing algorithm for compressible multicomponent problems, J. Comput. Phys. 142 (1998) 208.
[37] Strang, On the construction and comparison of difference schemes, SIAM J. Numer. Anal. 5 (3) (1968) 506–517.
[38] J. Thouvenin, Détonique, Collection du Commissariat à l'Energie Atomique, 1997 (in French).
[39] E.F. Toro, Riemann Solvers and Numerical Methods for Fluids Dynamics, Springer, Berlin, 1997.
[40] T.R. Young, A subroutine for solving stiff ordinary differential equations, Naval Research Laboratory memorandum Report 4091,Washington, DC, 1980.